

Nondimensional transport scaling in the Tokamak Fusion Test Reactor: Is tokamak transport Bohm or gyro-Bohm?

Cite as: Physics of Fluids B: Plasma Physics **5**, 477 (1993); <https://doi.org/10.1063/1.860534>

Submitted: 15 June 1992 . Accepted: 29 September 1992 . Published Online: 01 September 1998

F. W. Perkins, Cris W. Barnes, D. W. Johnson, S. D. Scott, M. C. Zarnstorff, M. G. Bell, R. E. Bell, C. E. Bush, B. Grek, K. W. Hill, D. K. Mansfield, H. Park, A. T. Ramsey, J. Schivell, B. C. Stratton, and E. Synakowski



View Online



Export Citation

ARTICLES YOU MAY BE INTERESTED IN

[Comparisons and physics basis of tokamak transport models and turbulence simulations](#)
Physics of Plasmas **7**, 969 (2000); <https://doi.org/10.1063/1.873896>

[Nondimensional transport scaling in DIII-D: Bohm versus gyro-Bohm resolved](#)
Physics of Plasmas **2**, 2342 (1995); <https://doi.org/10.1063/1.871259>

[Electron temperature gradient driven turbulence](#)
Physics of Plasmas **7**, 1904 (2000); <https://doi.org/10.1063/1.874014>



Nondimensional transport scaling in the Tokamak Fusion Test Reactor: Is tokamak transport Bohm or gyro-Bohm?

F. W. Perkins, Cris W. Barnes,^{a)} D. W. Johnson, S. D. Scott, M. C. Zarnstorff, M. G. Bell, R. E. Bell, C. E. Bush, B. Grek, K. W. Hill, D. K. Mansfield, H. Park, A. T. Ramsey, J. Schivell, B. C. Stratton, and E. Synakowski
Plasma Physics Laboratory, Princeton University, P. O. Box, 451, Princeton, New Jersey 08543

(Received 15 June 1992; accepted 29 September 1992)

General plasma physics principles state that power flow $Q(r)$ through a magnetic surface in a tokamak should scale as $Q(r) = \{32\pi^2 R r^3 T_e^2 c n_e a / [e B (a^2 - r^2)^2]\} F(\rho^*, \beta, \nu^*, r/a, q, s, r/R, \dots)$ where the arguments of F are local, nondimensional plasma parameters and nondimensional gradients. This paper reports an experimental determination of how F varies with normalized gyroradius $\rho^* \equiv (2T_e M_i)^{1/2} c / e B a$ and collisionality $\nu^* \equiv (R/r)^{3/2} q R \nu_e (m_e / 2T_e)^{1/2}$ for discharges prepared so that other nondimensional parameters remain close to constant. Tokamak Fusion Test Reactor (TFTR) [D. M. Meade *et al.*, in *Plasma Physics and Controlled Nuclear Fusion Research, 1990*, Proceedings of the 13th International Conference, Washington (International Atomic Energy Agency, Vienna, 1991), Vol. 1, p. 9] L-mode data show F to be independent of ρ^* and numerically small, corresponding to Bohm scaling with a small multiplicative constant. By contrast, most theories predict gyro-Bohm scaling: $F \propto \rho^*$. Bohm scaling implies that the largest scale size for microinstability turbulence depends on machine size. Analysis of a collisionality scan finds Bohm-normalized power flow to be independent of collisionality. Implications for future theory, experiment, and reactor extrapolations are discussed.

I. INTRODUCTION

What physics governs the flow of energy across magnetic surfaces in tokamaks? The prevailing theoretical picture^{1,2} is that microinstabilities, driven by density and temperature gradients, arise and create anomalous transport. By microinstabilities, we mean any process which creates density, temperature, velocity, or magnetic fluctuation structures with a spatial scale small compared to the tokamak as a whole and with a characteristic angular frequency comparable to the electron diamagnetic drift frequency. Because these instabilities have small spatial scales transverse to \mathbf{B} , one presumes their nonlinear saturation is controlled by local equilibrium quantities (e.g., n_e , T_e , B , q , etc.) and their gradients. It follows that heat and particle fluxes resulting from microinstabilities must also depend nonlinearly on local quantities and gradients, outside regions where global phenomena such as sawteeth³ and edge localized modes (ELM's)⁴ can affect heat transport.

A local, albeit nonlinear relation, between gradients and fluxes contrasts with the marginal stability picture^{5,6} of microinstability saturation. In this picture, the equilibrium temperature gradient relaxes to a value that puts ion-temperature-gradient modes just barely above their threshold,^{7,8} because otherwise a small deviation of the temperature gradient above its threshold value leads to very large heat fluxes. Hence, confinement scaling is governed by physics at the plasma periphery. Previously reported Tokamak Fusion Test Reactor⁹ (TFTR) data¹⁰ do not exhibit the sensitivity of heat flux to density profiles

predicted by marginal stability models. TFTR studies¹⁰ of plasma response to poloidal flux diffusion driven by current ramps find that temperature profiles and local transport throughout the plasma are insensitive to global current until poloidal flux diffusion has reached the $q \approx 1$ surface. If these results are to be understood in terms of local transport, then the electron heat flux must be independent of q and shear while the ion heat flux must decrease with increasing shear. In this paper, our working assumption is that a local relation is valid outside the sawtooth inversion radius.

In 1975, Kadomstev¹¹ observed that, through dimensional analysis based on fundamental plasma physics principles, it is possible to express the heat flow across a magnetic surface in terms of a diffusivity based on natural scale size $\rho_s \equiv (2T_e M_i)^{1/2} c / e B$ and time scale $\tau_0 \equiv L_n (M_i / 2T_e)^{1/2}$ of microinstabilities. The resultant diffusivity χ

$$\chi = \left(\frac{\rho_s^2}{\tau_0} \right) \frac{\bar{G}(\{p_i\})}{\langle k_{\perp} \rho_s \rangle} = \frac{(2T_e)^{3/2} M_i^{1/2} c^2 \bar{G}(\{p_i\})}{e^2 B^2 L_n \langle k_{\perp} \rho_s \rangle} \quad (1)$$

should govern the scaling properties of tokamak transport. Here $\bar{G}(\{p_i\})$ denotes a function of a set of local, nondimensional plasma parameters $\{p_i\}$ discussed below, and $\langle k_{\perp} \rho_s \rangle$ represents an average turbulent wave number normalized by the ion gyroradius. Note also that τ_0 is the inverse of the electron diamagnetic drift frequency evaluated at $k_{\perp} \rho_s = 1$ and that $\tau_0 = \Omega_i^{-1} (L_n / a \rho^*)$ scales inversely with gyrofrequency when nondimensional parameters remain fixed.

The explicit diffusivity, Eq. (1), has become known as gyro-Bohm and represents the transport scaling which nat-

^{a)}Permanent address: Los Alamos National Laboratory, Los Alamos, New Mexico 87545.

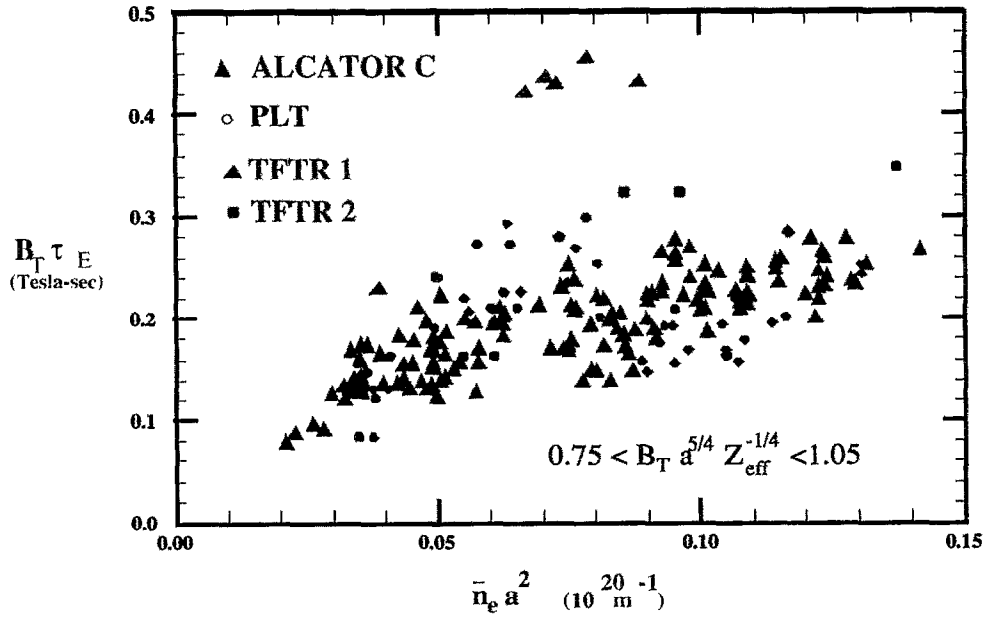


FIG. 1. Normalized global confinement time versus normalized density for discharges with a narrow range of normalized toroidal field $0.75 < B_N < 1.05$. TFTR-1 denotes discharges with an aspect ratio similar to Alcator-C and TFTR-2 discharges with an aspect ratio similar to PLT. (See Table II.)

urally results from fine-scale, collisionless, electrostatic microinstability modes.¹² However, this scaling rests on a concept of turbulence with a well-defined value of $\langle k_{\perp} \rho_s \rangle$, a concept which this paper examines experimentally.

Let us remark that power flow, not diffusivity, is the fundamental quantity for microinstability transport. Diffusivity introduces an arbitrary division of the factors involving gradients into their role in creating an anomalous diffusivity and in expressing the heat flux. A more general

statement equivalent to Eq. (1) is that the power flow through a magnetic surface takes the form

$$Q(r) = 32\pi^2 \sqrt{2} \frac{n_e T_e^{5/2} M_i^{1/2} c^2}{e^2 B^2} \left(\frac{r^3 R}{(a^2 - r^2)^2} \right) \frac{G(\{p_i\})}{\langle k_{\perp} \rho_s \rangle}. \quad (2)$$

We argue that G should be a nonlinear function of gradients because, in their absence, transport anomalies vanish. Let us introduce a common nondimensional definition of gradients,

$$\alpha_n \equiv -\frac{(a^2 - r^2)}{2rn_e} \frac{dn_e}{dr}, \quad \alpha_T \equiv -\frac{(a^2 - r^2)}{2rT} \frac{dT}{dr}. \quad (3)$$

For gyro-Bohm scaling, G is envisioned to have the general form

TABLE I. Eighteen nondimensional parameters.

Definition	Comment
$\rho^* = (2T_e M_i)^{1/2} c / e B a$	normalized gyroradius
$\beta = 8\pi n_e (T_e + T_i) / B^2$	plasma pressure
$\nu_e^* = \nu_e (m_e / 2T_e)^{1/2} (qR)^{5/2} / r^{3/2}$	collisionality
$q = rB / RB_{\theta}$	rotational transform
$s = rq' / q$	magnetic shear
$\alpha_n = -[(a^2 - r^2) / 2rn_e] (dn_e / dr)$	density profile shape
$\alpha_T = -[(a^2 - r^2) / 2rT_e] (dT_e / dr)$	temperature profile shape ^a
T_e / T_i	temperature ratio
Z_{eff}	impurity concentration
r/R	local toroidicity
r/a	relative minor radius
$\nu_{ie} T_E$	temperature equilibration; beam slowing down
$Q(r)/P$	power deposition profile
E_{beam} / T_e	beam injection energy
$\nu_{ion} n_0 \tau_p / n_e$	particle fueling profile
κ, δ	plasma elongation, triangularity
M_i / m_e	mass ratio
P_{rad} / P	radiated power fraction

^aThe well-known parameter $\eta_i = \alpha_T / \alpha_n$.

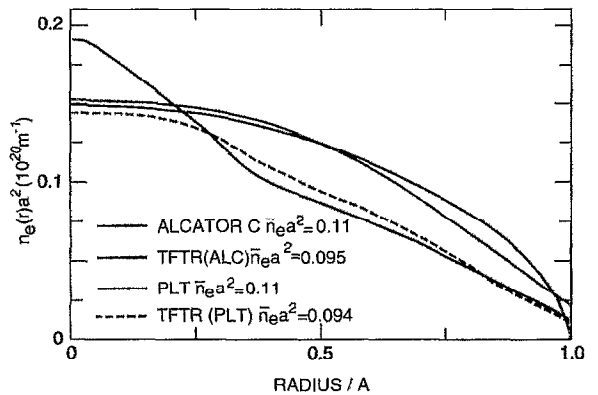


FIG. 2. Density profiles measured on Alcator-C, PLT, and TFTR for almost constant $\bar{n}_e a^2$ and $B_N = B_T a^{5/4} Z_{eff}^{-1/4}$.

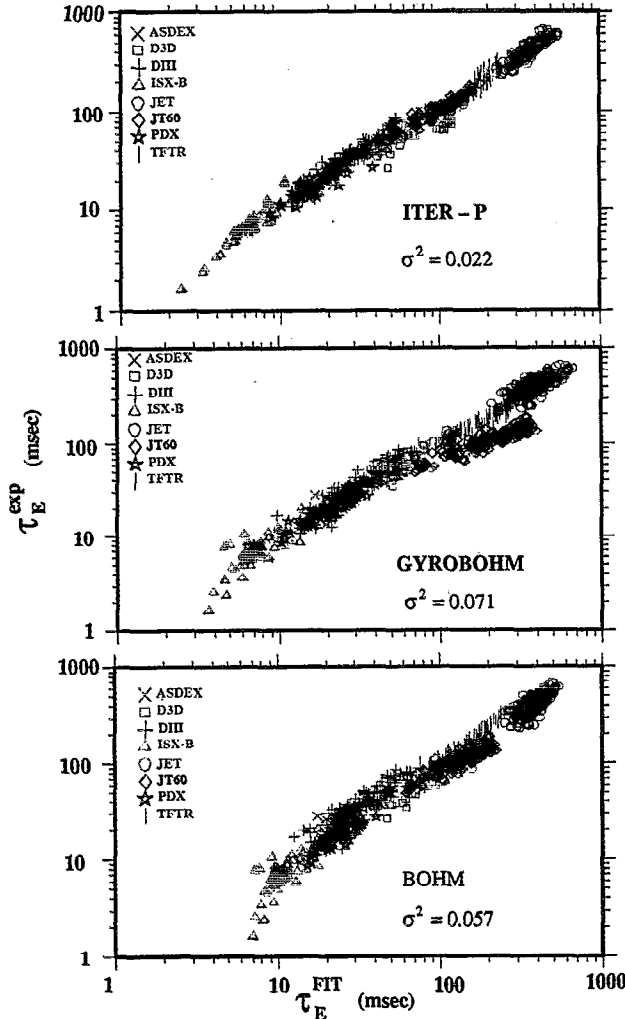


FIG. 3. Experimental global L-mode confinement times versus three fits, ITER-P, gyro-Bohm, and Bohm given in Eqs. (16)–(18). Here σ^2 denotes the relative mean square deviation of the data from the fit. These graphs provided by S. Kaye. Consult Ref. 47 for a description of the database.

$$G = G_1 \alpha_n^2 + G_2 \alpha_n \alpha_T + G_3 \alpha_T^2,$$

where the G_n can depend on other nondimensional parameters such as q .

In this paper, we compare experimental results to the generalized gyro-Bohm power flow expression Eq. (2) and the corresponding Bohm scaling expression

$$Q_{\text{Bohm}}(r) = 32\pi^2 \frac{n_e T_e^2 c a}{e B} \left[\frac{r^2 R}{(a^2 - r^2)^2} \right] F(\{p_i\}), \quad (4)$$

where $F = \rho^* G / \langle k_{\perp} \rho_s \rangle = G / \langle k_{\perp} a \rangle$ and we define ρ^* by

$$\rho^* \equiv \frac{\rho_s}{a} = \frac{\sqrt{2T_e M_i c}}{e B a}.$$

In addition to the explicit scaling on plasma parameters, the power flow expression Eq. (2) contains two important additional factors— $1/\langle k_{\perp} \rho_s \rangle$ and the nondimensional function $G(\{p_i\})$. The first factor measures the mean wave number of microinstability turbulence and de-

TABLE II. Nondimensionally identical tokamak discharges.

Quantity	Alcator-C	PLT	TFTR-1 ^a	TFTR-2 ^b
I_p (kA)	300–700 ^c	400–500	377	377
a (m)	0.165	0.40	0.73	0.83
R (m)	0.64	1.32	2.86	2.75
B_T (T)	9.2–1.04	3.2	1.53	1.27
$B_T a^{5/4} Z_{\text{eff}}^{-1/4}$ (T m ^{5/4})	0.81–1.05	0.85–1.05	0.76–0.83	0.78–0.85
\bar{n}_e (10 ²⁰ m ⁻³)	0.8–5.5	0.24–0.86	0.07–0.16	0.07–0.16
$\bar{n}_e a^2$ (10 ²⁰ m ⁻¹)	0.022–0.15	0.038–0.14	0.038–0.087	0.048–0.12

^aAspect ratio similar to Alcator-C.

^bAspect ratio similar to PLT.

^cAlcator-C data exhibited no dependence of $B_T \tau_E$ on plasma current.

termines whether Bohm or gyro-Bohm scaling prevails. The key issue is the following: Does $\langle k_{\perp} \rho_s \rangle$ depend on ρ^* ? Two limiting cases arise: First, if $\langle k_{\perp} \rho_s \rangle$ is independent of ρ^* , then the turbulent cell sizes in a tokamak depend only on relative local geometry (e.g., q , s , r/a , r/R) and gyro-radius. In this case, tokamak transport exhibits gyro-Bohm scaling and differs qualitatively from hydrodynamic turbulent heat transfer where eddies of size comparable to the system size dominate transport. For example, if one posits that a long-wavelength cutoff for microinstability turbulence occurs where the diamagnetic drift frequency becomes comparable to the ion bounce frequency, then $\langle k_{\perp} \rho_s \rangle \approx 2L_n r^{1/2}/qR^{3/2}$ could depend strongly on relative minor radius but not on absolute machine size. An example of the second limit is the *ad hoc* statement that $\langle k_{\perp} \rho_s \rangle \approx m_0 \rho_s / r$, which implies turbulent cell sizes scale with machine size, yielding a Bohm scaling of confinement. Here m_0 denotes a number that can depend on relative geometry such as q , r/R , etc., but is independent of absolute size. Furthermore, m_0 must be large to agree with the observed magnitude of tokamak transport. Most direct statements of the long-wavelength cutoff for microinstabilities result in gyro-Bohm scaling.¹³ Low-mode-number trapped-ion modes¹⁴ could potentially be consistent with Bohm scaling, but attempts¹³ to find a self-consistent, nonlinear spectrum for trapped-ion modes have led to gyro-Bohm expressions for the diffusivity. Recently, Tang and Rewoldt¹⁵ have numerically computed linear trapped-ion mode eigenfunctions that extend over many rational surfaces, in contrast to earlier work.¹⁶ Extended eigenfunctions are a requisite for Bohm transport scaling.

There are two approaches to determining experimentally whether the spectrum of microinstability turbulence depends on absolute machine size: direct measurement of density fluctuation spectra and observations of confinement scaling consequences. This paper reports TFTR scaling data which exploit the second approach. With regard to the first approach, microwave scattering experiments¹⁷ suffer from poor spatial resolution as $k_{\perp} \rho_s$ becomes small, preventing a direct measurement of the long-wavelength cutoff by this technique. Fortunately, incoherent measurements of fluctuations, such as beam emission spectroscopy,¹⁸ are being developed for the first approach.

The function $G(\{p_i\})$ in Eqs. (1) and (2) indicates that, in addition to the explicit scaling, microinstability

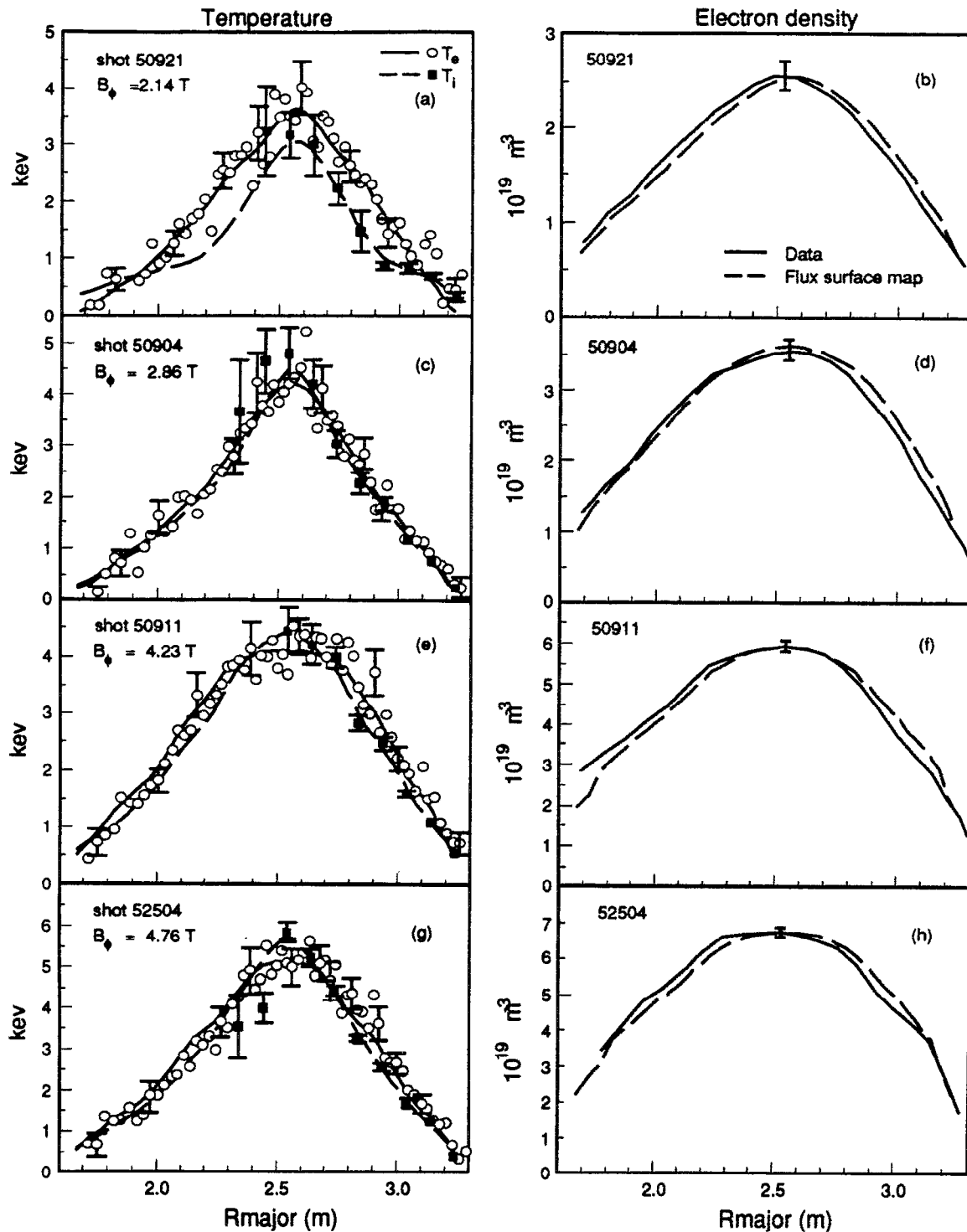


FIG. 4. Density and temperature profile data versus major radius for shots in the low-density ρ^* scan. Electron temperatures are from Thomson scattering and ion temperatures from CHERS.⁵³ Electron densities deduced by inversion of eight-channel interferometer data are shown by solid curves and the flux-surface mapped densities, used in our data analysis, by dashed curves.

diffusivities can depend on local, nondimensional plasma parameters denoted by $\{p_i\}$ and defined in Table I. Thus, the density gradient scale length appearing in Eq. (1) is not fundamental. Nondimensional factors can readily transform it into a pressure gradient scale length, temperature gradient scale length, etc. Nondimensional param-

eters further allow for stochastic magnetic fluctuation transport. The list of such parameters is unfortunately long, and they can act as hidden variables in confinement parameter scans, complicating their interpretation. For example, the electron-ion temperature equilibrium parameter $v_{ie}\tau_E$ and power deposition profile $Q(r)/P$ vary during a scan in

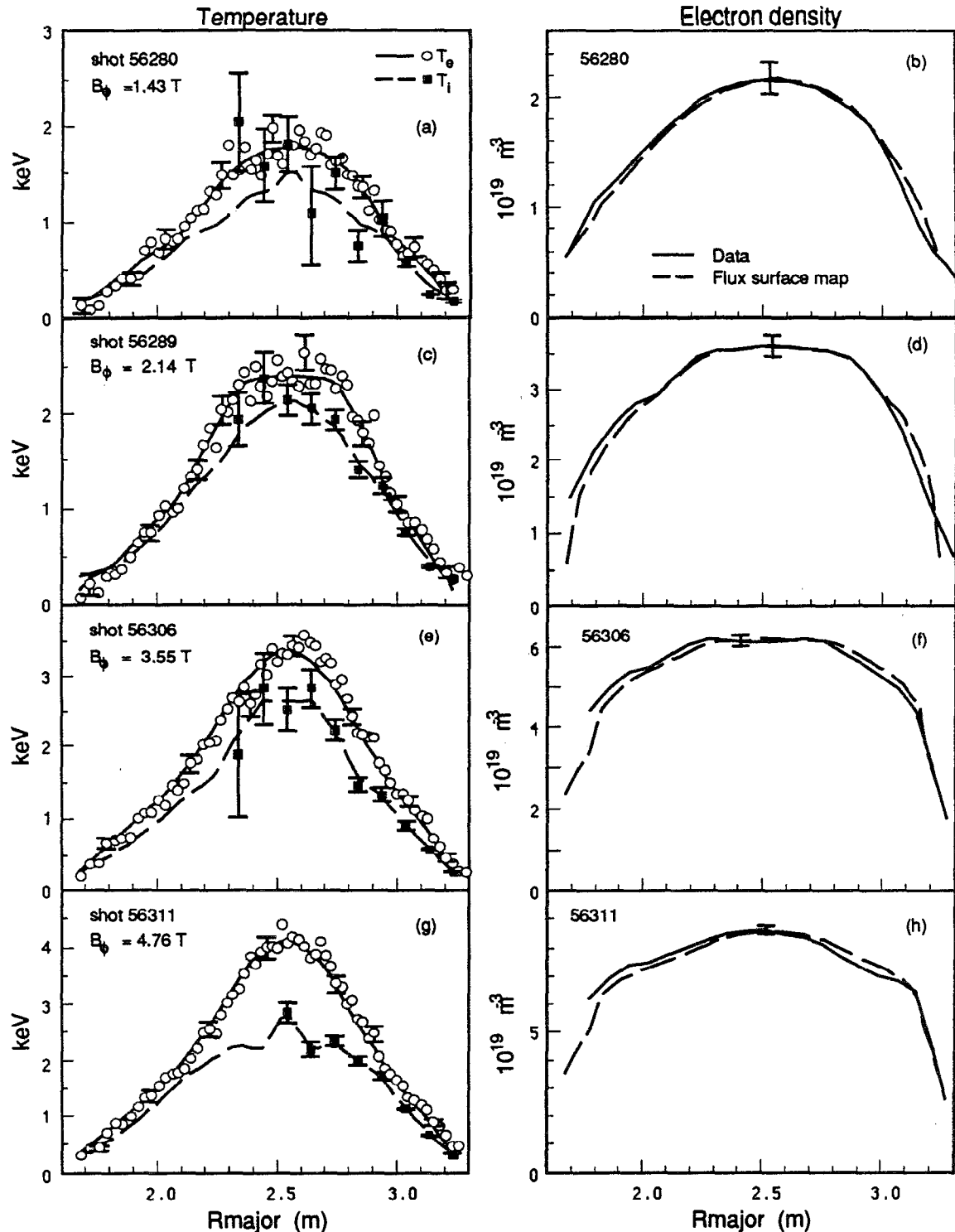


FIG. 5. Density and temperature profile data versus major radius for shots in the high-density ρ^* scan. Electron temperatures are from Thomson scattering and ion temperatures from CHERS.⁵³ Electron densities deduced by inversion of eight-channel interferometer data are shown by solid curves and the flux-surface mapped densities, used in our data analysis, by dashed curves.

which the density increases, thereby constituting a potential source of bias in the density dependence of thermal energy confinement. In our work, the use of local power flow eliminates the power deposition effect. Because our analysis involves only combined electron and ion power flows, electron-ion equilibration does not enter directly.

Further, electron-ion equilibration is sufficient (for most shots) to maintain T_e/T_i close to unity, eliminating systematic variation in T_e/T_i as a hidden variable in confinement scaling. The experimental results presented in the body of this paper rest on a sequence of discharges controlled so as to minimize variations in all nondimensional

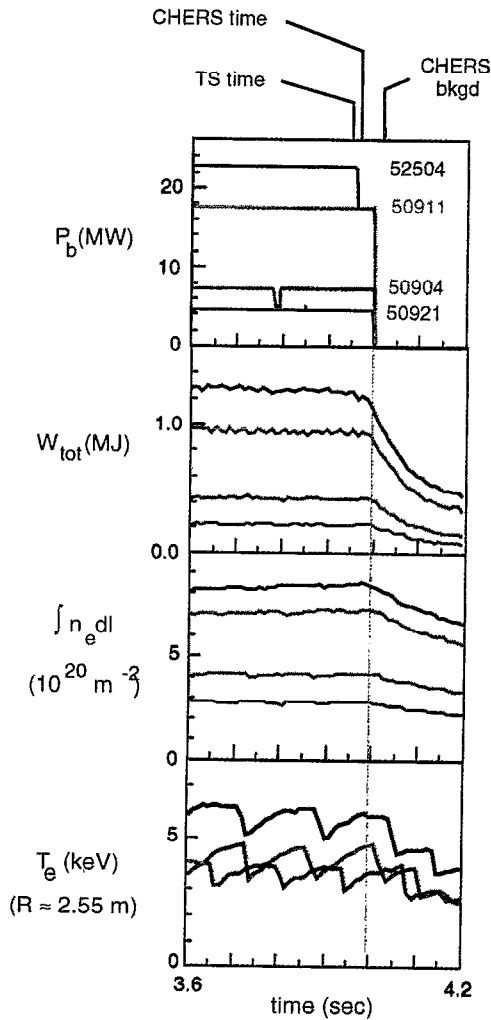


FIG. 6. Waveforms for shots in the low-density ρ^* scan.

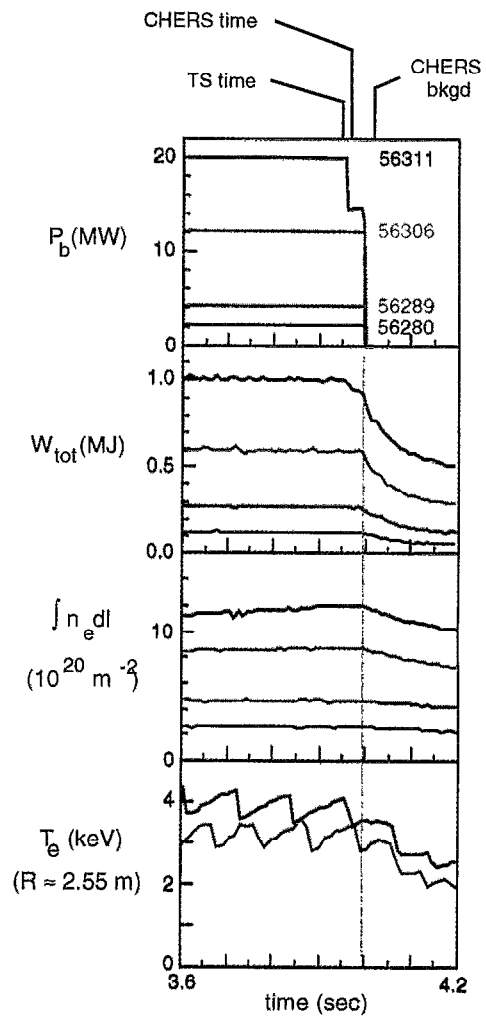


FIG. 7. Waveforms for shots in the high-density ρ^* scan.

parameters except ρ^* (or ν^* in one scan). It is difficult, with limited experimental time to accomplish this for 17 parameters simultaneously and it is unintended variations in nondimensional parameters that contribute the greatest uncertainty to our conclusions.

Our confidence in projecting performance of future fusion devices will be increased if these projections are based on experimentally validated theoretical principles, even though normalizing constants are obtained via fits to data.¹⁹ In this context, scaling of confinement with normalized gyroradius ρ^* is of particular interest to magnetic fusion research because one can create in present-shaped tokamaks, such as the Doublet III-D tokamak²⁰ (DIII-D) and Joint European Torus²¹ (JET), discharges which have all nondimensional parameters, apart from ρ^* , identical to discharges anticipated for the Burning Plasma Experiment²² (BPX) and International Thermonuclear Experimental Reactor²³ (ITER). Thus extrapolating present confinement data to ITER and BPX is equivalent to extrapolation in the parameter ρ^* .

This paper reports a study of the ρ^* and ν_e^* dependence of confinement in L-mode TFTR discharges. Two

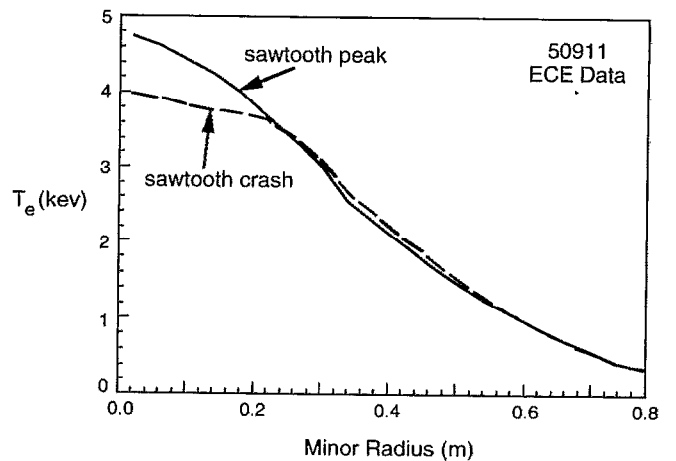


FIG. 8. ECE electron temperature versus minor radius for shot 50911 from the low-density ρ^* scan. These traces show the inversion radius to be $r=0.24$ m and show negligible sawtooth effect on T_e for $r>0.24$ m.

TABLE III. Nondimensional parameter scans ($R=2.45$ m, $a=0.80$ m).

Shot	B_T (T)	I_p (MA)	\bar{n}_e (10^{19} m $^{-3}$)	$T_e(0)$ (keV)	$\rho^*(0)$	$(v_e^*)_{\min}$ ^a	$\bar{\beta}$ ^b	P_{MW} ^c	τ_E (sec)	q	Z_{eff}
Low-density ρ^* scan											
50921	2.14	0.89	1.8	3.6	0.0070	0.05	0.0055	2.9	0.071	3.1	2.4
50904	2.86	1.19	2.7	4.3	0.0057	0.06	0.0049	5.2	0.081	3.1	2.1
50911	4.22	1.78	4.5	4.2	0.0038	0.06	0.0047	12.0	0.081	3.1	2.4
52504	4.76	1.98	5.2	5.2	0.0038	0.06	0.0046	16.4	0.078	3.1	2.3
High-density ρ^* scan											
56280	1.42	0.59	1.6	1.8	0.0075	0.09	0.0055	1.5	0.086	3.1	1.2
56289	2.14	0.89	2.9	2.4	0.0057	0.09	0.0053	3.3	0.094	3.1	1.5
56306	3.55	1.48	5.3	3.4	0.0041	0.12	0.0040	9.2	0.080	3.1	1.6
56311	4.76	1.98	7.3	4.1	0.0034	0.10	0.0036	15.3	0.081	3.1	1.6
v^* scan											
50890	1.43	0.59	2.1	1.7	0.0072	0.19	0.0055	1.7	0.081	3.1	1.8
52527	2.15	0.89	2.3	2.8	0.0063	0.08	0.0051	3.4	0.074	3.1	1.9
50903	2.86	1.19	2.2	4.5	0.0059	0.05	0.0065	5.5	0.074	3.1	2.7
50862	3.55	1.48	2.5	5.8	0.0053	0.04	0.0071	9.2	0.066	3.1	3.9

^aMinimum value of v_e^* versus minor radius.^b $\bar{\beta}=8\pi\langle n_3(T_e+T_i)\rangle_{vol}/B^2$.^cThermal powerflow.

sequences of discharges were prepared which held all nondimensional parameters approximately constant except for ρ^* , as well as one sequence in which just v_e^* varied. To avoid complications resulting from a varying power deposition profile, the comparison between various members of the scan is done in terms of a nondimensional power flow through a magnetic surface. We also compare data from the Princeton Large Torus²⁴ (PLT) and Alcator-C²⁵ tokamaks to TFTR results to examine whether discharges with all nondimensional parameters fixed exhibit constant Ω/τ_E as predicted by the general principles of Sec. II.

A similar ρ^* scaling investigation was carried out on the DIII-D tokamak²⁶⁻²⁹ with results that differed from those reported below. Where could the differences lie? As is true for TFTR experiments, the interpretation of DIII-D data relies on an accurate knowledge of the power deposition profile. However, the sawtooth mixing radius lies at $r/a \approx 0.5-0.6$ in DIII-D³ and sawtooth periods are comparable to beam slowing down times.³⁰ Hence sawteeth could entrain energetic ions and alter the power deposition profile. In TFTR, this process has been shown to affect power deposition profiles for ion cyclotron range of frequency (ICRF) heating.³¹ In this paper, we restrict our analysis to the region outside the sawtooth mixing radius (see Fig. 8). Furthermore, the requirement that all nondimensional parameters, except ρ^* , remain fixed is not easily met in a real TFTR scan. In particular, the density profile shape α_n and temperature ratio T_e/T_i parameters are difficult to control. The equilibrium parameter $\langle v_{ie} \rangle \tau_E$ systematically varies as $(\rho^*)^{-n}$ with $n=1$ for Bohm scaling and $n=2$ for gyro-Bohm in ρ^* scans. The most recent DIII-D attempts^{28,29} to control the power deposition profile experienced similar difficulties. In accord with the TFTR data presented in this paper, the recent DIII-D confinement results are consistent with Bohm scaling. Our research, and that of the DIII-D

team, constitute the most definitive efforts to eliminate systematic variation of one nondimensional parameter with another and thereby avoid ambiguities in confinement scaling. Additional experiments will be required to address points of difference which remain between TFTR and DIII-D.

The paper turns in Sec. II to the question of what natural space and time scales result from casting the equations governing nonlinear microinstabilities into nondimensional form. It is argued that fine-scale instabilities correspond to gyro-Bohm scaling whereas longer wavelength modes produce Bohm scaling. Section III examines whether global confinement times in Ohmic discharges with nondimensional parameters constant obey the scaling $\tau_E \propto \Omega_i^{-1}$ which follows from the considerations of Sec. II. Section IV asks whether existing global confinement databases can distinguish between Bohm and gyro-Bohm scaling. Section V presents the main results: Power flow across magnetic surfaces in TFTR normalized according to Bohm, gyro-Bohm, and Goldston scaling relations. Particular attention is paid to the magnitude of unintended variation in nondimensional parameters. A discussion concludes the paper.

II. NONDIMENSIONAL THEORY

Two decades of research^{1,32-34} on linear stability of fine-scale modes in tokamaks show that they are invariably unstable over an appreciable wave-number range. Confinement consequences are expected, but linear theory cannot predict which class of modes will dominate transport physics. However, considerable insight can be gained simply by casting the nonlinear equations governing microinstabilities into nondimensional form.

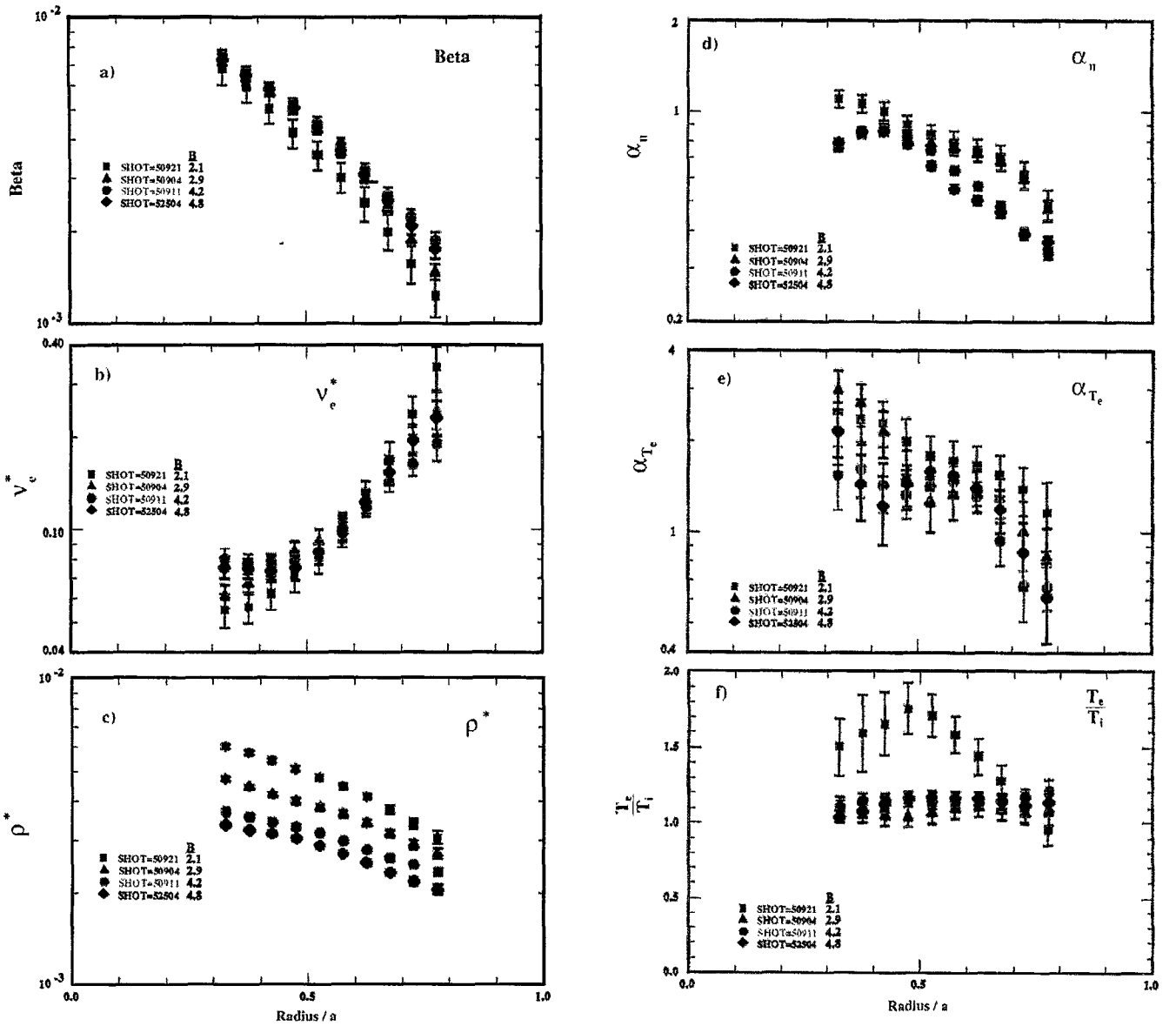


FIG. 9. Nondimensional parameters plotted against minor radius for the low-density ρ^* scan.

Natural length and time scales for microinstability turbulence emerge from a scaling of both independent and dependent variables. For example, in the case of sheared slab geometry, the nondimensional, nonlinear ion fluid equations take the form

$$\frac{\partial n}{\partial \tau} + \frac{\partial \phi}{\partial \tau} - \left(\frac{\partial}{\partial \tau} - (1 + \eta_i) \frac{\partial}{\partial y} \right) \nabla^2 \phi + \nabla_{\parallel} v = -[\phi, n] + [\phi, \nabla^2 \phi], \quad (5)$$

$$\frac{\partial v}{\partial \tau} + \nabla_{\parallel} (\phi + p) = -[\phi, v], \quad (6)$$

$$\frac{\partial p}{\partial \tau} + \frac{(1 + \eta_i)}{(T_e/T_i)} \frac{\partial \phi}{\partial y} = -[\phi, p], \quad (7)$$

with

$$[A, B] = \frac{\partial A}{\partial x} \frac{\partial B}{\partial y} - \frac{\partial A}{\partial y} \frac{\partial B}{\partial x} \quad (8)$$

in a recent review by Horton.³⁵ Here

$$n = \frac{L_n}{\rho_s} \left(\frac{\tilde{n}}{n_0} \right), \quad \phi = \frac{L_n}{\rho_s} \left(\frac{e\tilde{\Phi}}{T_e} \right), \quad x_{\perp} = \frac{r_{\perp}}{\rho_s}, \quad \tau = t \frac{c_s}{L_n}, \quad (9)$$

$$p = \frac{L_n}{\rho_s} \left(\frac{\tilde{p}}{p_0} \right), \quad v = \frac{L_n}{\rho_s} \left(\frac{v_{\parallel}}{c_s} \right), \quad \nabla_{\parallel} = \left(\frac{L_n}{B} \right) \mathbf{B} \cdot \nabla, \quad c_s = \left(\frac{T_e}{M_i} \right)^{1/2}, \quad (10)$$

denote scaled nondimensional variables. A similar scaling³⁶ transforms nonlinear kinetic equations into a nondimensional form involving only nondimensional parameters of

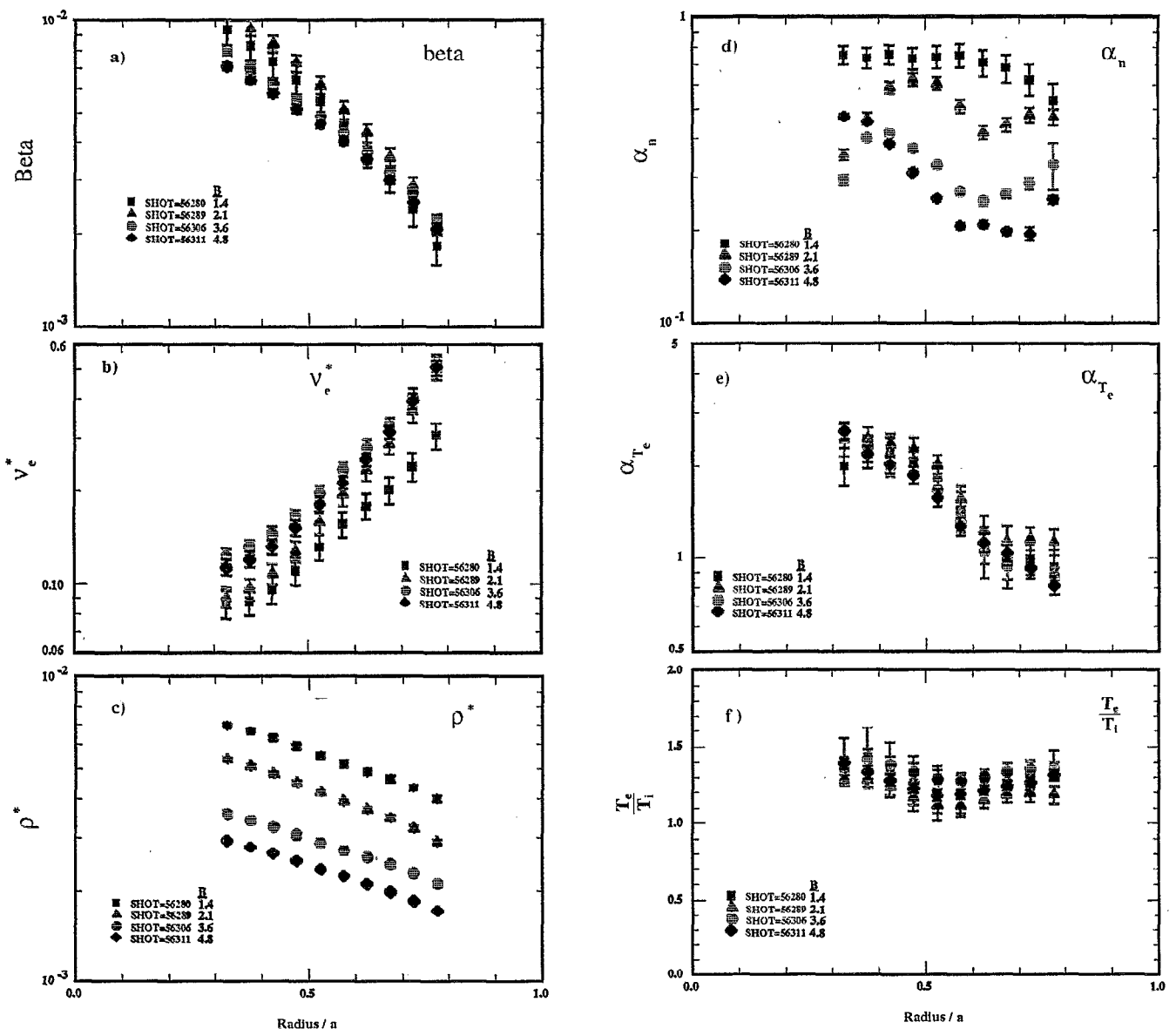


FIG. 10. Nondimensional parameters plotted against minor radius for the high-density ρ^* scan.

order unity. When Fourier transforms are used in the y and z directions, ∇_{\parallel} takes the form

$$\nabla_{\parallel} \rightarrow i(k_y)_m (x - x_{m,n}) \frac{L_n}{L_s}, \quad (11)$$

where $x_{m,n}$ denotes a rational surface. Connor's treatment³⁷ of ion-temperature-gradient turbulence has similar equations. Nondimensional equations can also be derived for fluid electrons³⁵ and a generalization to an electron kinetic equation is straightforward.³⁸

We wish to make three points: First, the characteristic length and time scales of microinstability turbulence arise from a scaling of the equation governing nonlinear drift waves into a nondimensional form where all coefficients are of order unity. Hence, the corresponding gyro-Bohm diffusivity is more fundamental than the customary γ/k_{\perp}^2

estimates. Second, the magnetic shear length L_s enters through ∇_{\parallel} in a way whose scaling consequences are not transparent, as does toroidicity in toroidal geometry.³⁹ Third, the nonlinear terms have high derivatives [fourth order; see Eq. (5)] and hence are weak for long wavelength modes. An increase in mode amplitude at long wavelength is expected and its precise form will determine whether Bohm or gyro-Bohm scaling prevails.

In brief, casting the equations governing microinstabilities into their simplest mathematical form, Eqs. (5)–(10), naturally introduces the time and space scales characteristic of microinstability transport and provides an understanding of why fluctuation amplitudes increase with wavelength. Scaling with nondimensional parameters such as s , q , η_p , r/R , etc., is not simple and bifurcations are a possibility.

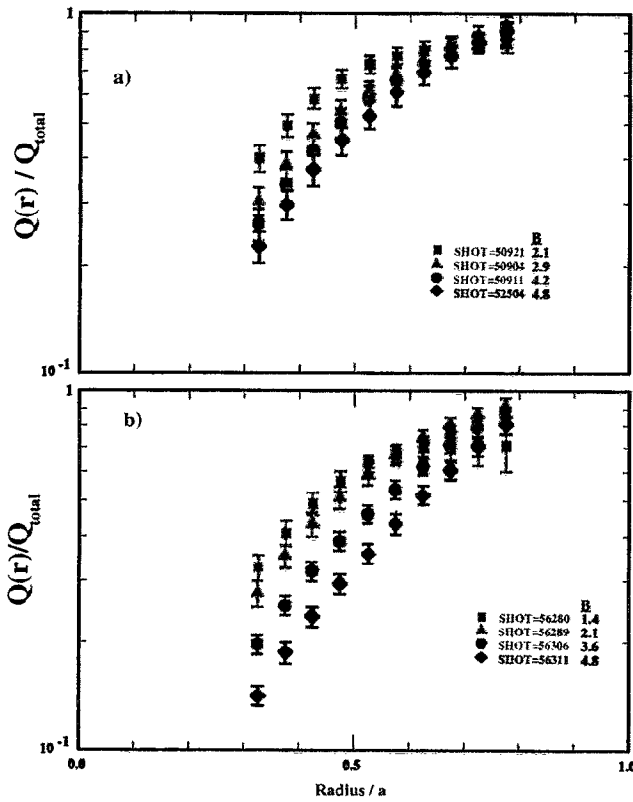


FIG. 11. Relative power flow profiles for ρ^* scans (a) low-density ρ^* scan, (b) high-density ρ^* scan. The thermal power flow $Q(r)$, which is defined to be the power deposited inside a given magnetic surface in the thermal plasma by beams, Ohmic heating, and beam thermalization less radiative and charge exchange losses, is normalized by the total power Q_{total} deposited in the thermal plasma.

III. NONDIMENSIONALLY IDENTICAL OHMIC DISCHARGES

Are observed tokamak confinement times consistent with the principles set forth above? A key test is to investigate confinement scaling in a sequence of tokamak discharges in which all nondimensional parameters of Table I are arranged to be identical. In such a sequence, the characteristic time scale

$$\tau_0 = \frac{L_n}{c_s} = \left(\frac{1}{\Omega_i} \right) \left(\frac{L_n}{a \rho^*} \right) = \left(\frac{1}{\Omega_i} \right) \left(\frac{(a^2 - r^2)}{2 \rho^* r a \alpha_n} \right) \quad (12)$$

scales inversely with gyrofrequency. Hence the confinement time, which is related to τ_0 through nondimensional parameters [e.g., $\tau_E \propto \tau_0 (\rho^*)^{-2}$ for gyro-Bohm scaling], must scale inversely with gyrofrequency. Constancy of the three parameters ν^* , ρ^* , and β require the density, temperature, and magnetic fields in two discharges (denoted by 1 and 2) of different minor radius a to be related by

$$n_2 = n_1 \left(\frac{a_1}{a_2} \right)^2, \quad B_2 = B_1 \left(\frac{Z_{\text{eff},2}}{Z_{\text{eff},1}} \right)^{1/4} \left(\frac{a_1}{a_2} \right)^{5/4}, \quad (13)$$

$$T_2 = T_1 \left(\frac{Z_{\text{eff},2}}{Z_{\text{eff},1}} \right)^{1/2} \left(\frac{a_1}{a_2} \right)^{1/2}.$$

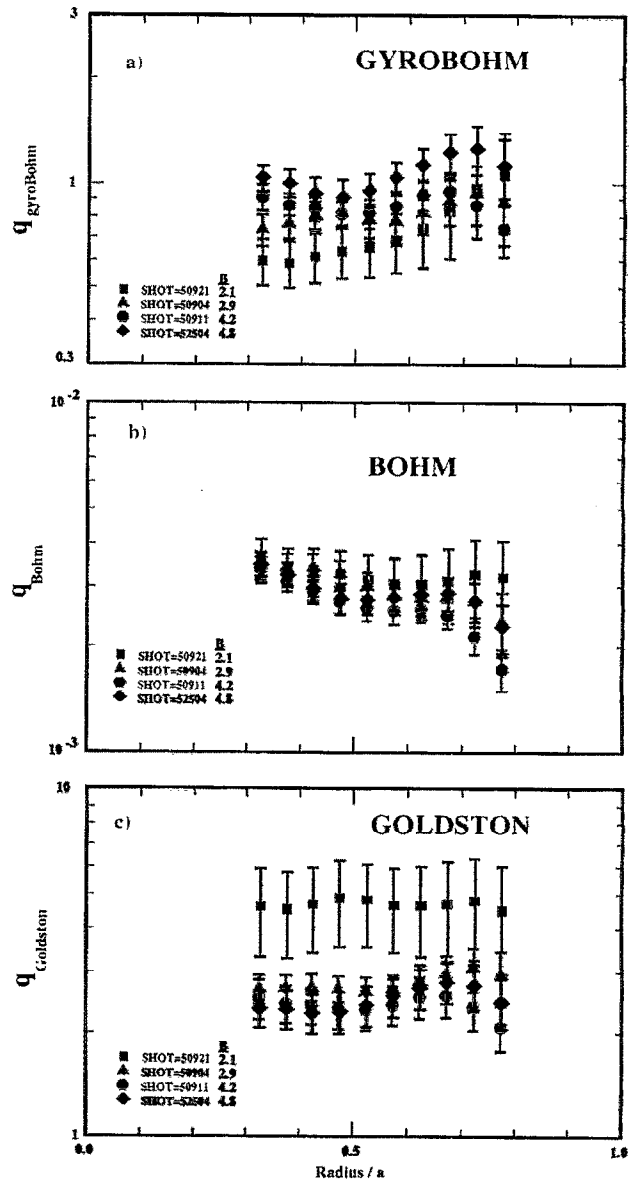


FIG. 12. Bohm, gyro-Bohm, and Goldston normalized power flow for the low-density ρ^* scan. Error bars in this figure represent the standard deviation of many calculations of normalized power flow, each of which has input data distributed about the measured value according to a Gaussian distribution whose standard deviation is the estimated experimental random error. A triangular radial profile smoothing of full width at half-maximum of 10 cm is then applied.

We assume that other parameters dependent on profile shapes can be held fixed. For meaningful experimental-theoretical comparison, one must examine the constancy of nondimensional parameters as well as the normalized confinement time.

Ohmic discharges, in contrast to those heated by neutral beam injection (NBI), have the advantage that the relative power deposition profile remains effectively constant even though density varies by more than an order of magnitude. Of course, temperature cannot be independently controlled in Ohmic discharges. But from the relations valid for Ohmic plasmas,

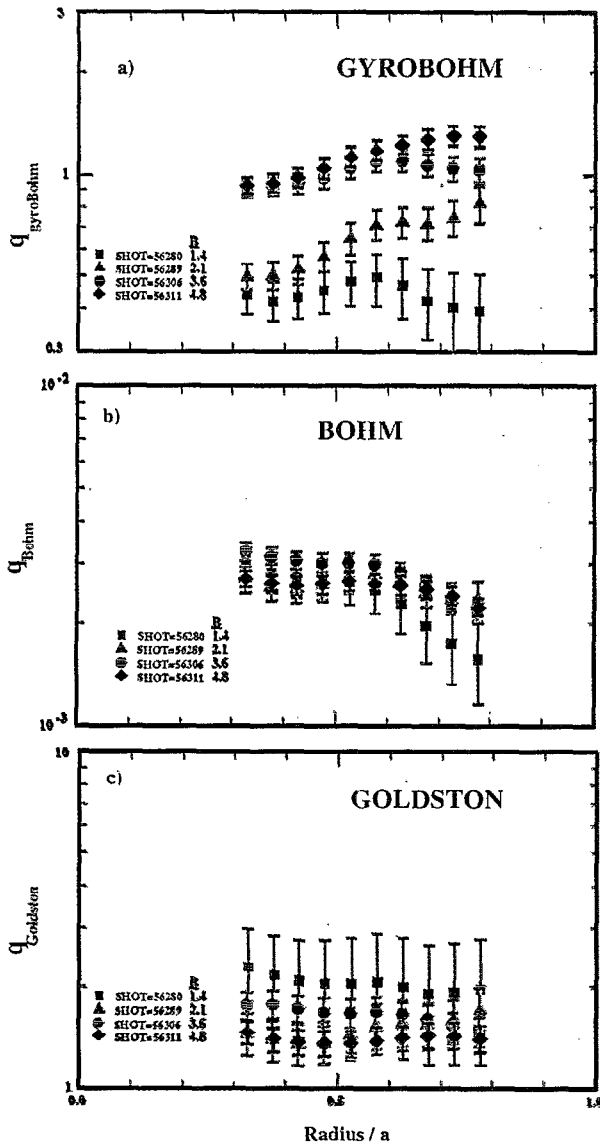


FIG. 13. Bohm-, gyro-Bohm-, and Goldston-normalized power flow for the high-density ρ^* scan. Error bars in this figure represent the standard deviation of many calculations of normalized power flow, each of which has input data distributed about the measured value according to a Gaussian distribution whose standard deviation is the estimated experimental random error. A triangular radial profile smoothing of full width at half-maximum of 10 cm is then applied.

$$\tau_E \propto \frac{nT_e R a^2}{P_\Omega}, \quad P_\Omega = VI_p \propto \frac{B_T^2 a^2 Z_{\text{eff}}}{q_a R T_e^{3/2} q(0)}, \quad (14a)$$

$$V = \frac{4\pi B_T \eta(0)}{\mu_0 q(0)} = j(0) \eta(0) 2\pi R, \quad I_p = \frac{2\pi a^2 B_T}{\mu_0 R q_a}, \quad (14b)$$

where $\eta(0)$ denotes the on-axis resistivity, one can directly see that if $B_T \tau_E$ remains constant, the temperature scaling required in Eq. (13) will follow, provided n_e and B_T have been scaled according to Eq. (13). Conversely, if the confinement time does not scale inversely with magnetic field, then the temperature will not fulfill the scaling expressed in Eq. (13) for an Ohmic discharge.

To test these plasma physics principles, two TFTR density scans were carried out with toroidal field and electron density values selected to correspond to PLT and Alcator-C data through scaling principles Eq. (13). The TFTR scans differed in aspect ratio and q_a to match PLT and Alcator-C. Normalized confinement in Alcator-C is essentially independent of q_a . The scans called for discharges with toroidal field and plasma current values well below TFTR's usual operating range. Table II lists parameters for shots in Alcator-C,²⁵ PLT,²⁴ and TFTR which fulfill scaling requirements Eq. (13). The TFTR discharges were run on an outside limiter called the rf limiter. Figure 1 presents normalized global confinement times versus normalized density, for effectively fixed normalized toroidal field B_N , defined according to

$$B_N = \left(\frac{B}{1 \text{ T}} \right) \left(\frac{a}{1 \text{ m}} \right)^{5/4} Z_{\text{eff}}^{1/4}.$$

If all nondimensional parameters are constant and plasma physics principles govern confinement, the points from the three machines should form a single curve. Agreement is good for Alcator-C and PLT, as reported previously.⁴⁰ While the "PLT-like" TFTR discharges are within uncertainties of the older data, the "Alcator-C-like" discharges show distinctly improved confinement.

Were all nondimensional parameters fixed? Unfortunately, the density profile shape was not readily controlled and is influenced by atomic physics as well as plasma physics. Figure 2 shows TFTR density profiles to be distinctly steeper than the corresponding ones of Alcator-C and PLT. Taken together, Figs. 1 and 2 exhibit a distinct correlation between improved normalized confinement time $\Omega_i \tau_E$ and density profile peaking. Apparently the Alcator-C-like TFTR discharges are similar to the improved Ohmic confinement (IOC) regime discovered by the ASDEX tokamak⁴¹ (Axially Symmetric Divertor Experiment) and characterized by steep, self-maintained density profiles. One possibility is that the IOC regime is controlled by the particle fueling profile. Low-energy Frank-Condon neutral atoms are somewhat more likely to charge exchange than ionize in the plasma periphery,⁴² thus giving neutral atoms a velocity comparable to plasma ions. The normalized mean-free path for electron impact ionization⁴³ λ_i/a for such neutrals is approximately given by

$$\frac{\lambda_i}{a} \approx (0.12) \left(\frac{10^{19} \text{ m}^{-1}}{n_e a^2} \right) \left(\frac{a}{1 \text{ m}} \right) \left(1.0 + \frac{T_e}{100 \text{ eV}} \right)^{1/2} \ll 1, \quad (15)$$

so the particle source is confined to the edge region of all tokamaks, even though the relative penetration distance changes appreciably. Expression (15) is a nondimensional parameter involving atomic physics (i.e., physics, beyond plasma physics principles) and necessarily varies even though n_e , a , and B_T are arranged via Eq. (13) to maintain plasma nondimensional parameters constant. Other possibilities involve the level of neutral gas pressure at the plasma periphery, which influences ionization and radiation loss rates, and their effect on microinstabilities⁴⁴⁻⁴⁶ and transport.⁴⁷

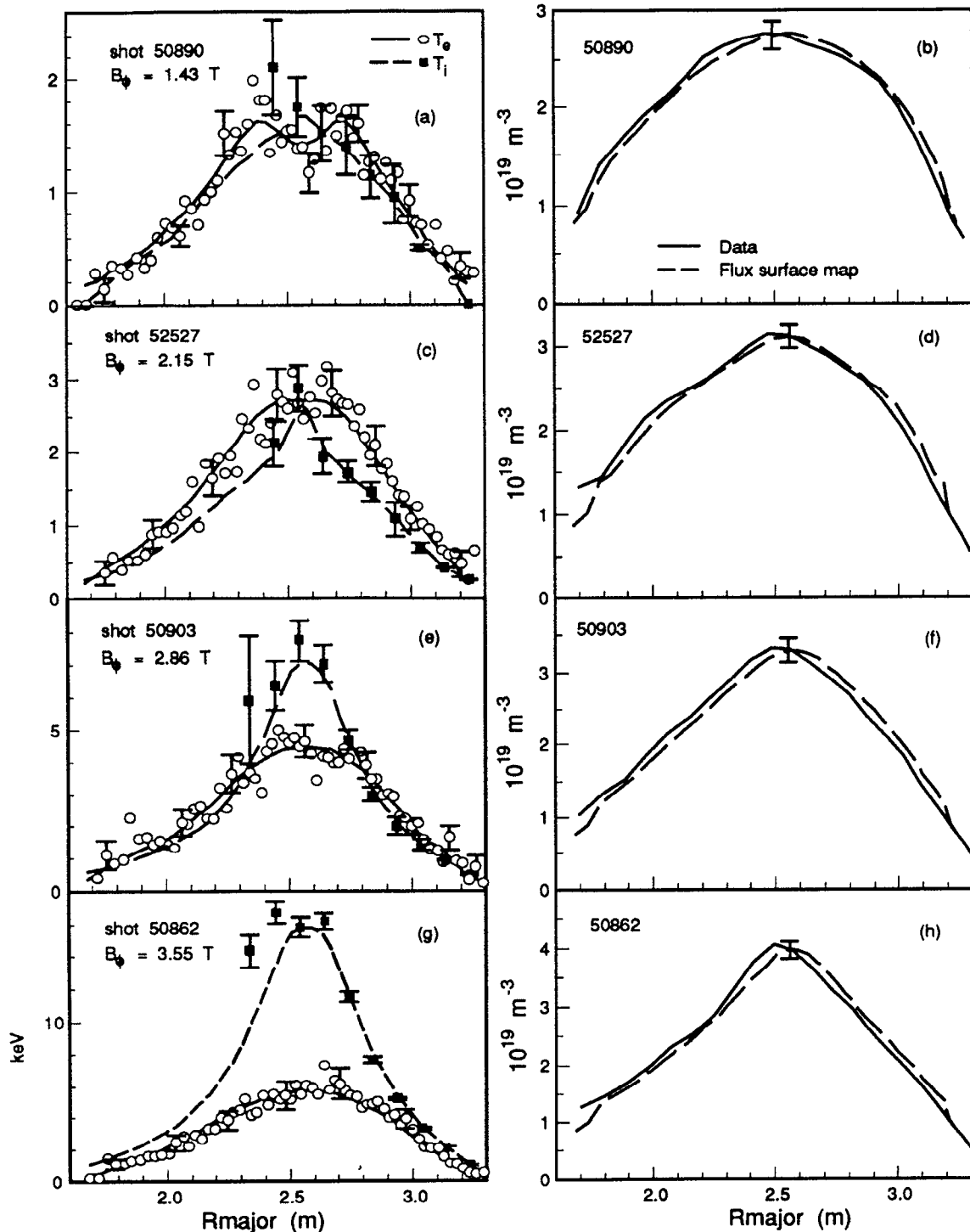


FIG. 14. Density, electron temperature, and ion temperature versus major radius for the ν^* scan. Electron temperatures are from Thomson scattering and ion temperatures from CHERS.⁵³ Electron densities deduced by inversion of eight-channel interferometer data are shown by solid curves and the flux-surface mapped densities, used in our data analysis, by dashed curves.

Our results point out that, in common with many previous studies, tokamak transport can exhibit bifurcations which nondimensional parameters control. Some bifurcations, such as transitions to H-mode and IOC regimes, are large and recognized. Others are probably not yet identified and constitute hidden variables in confinement scaling

relations. From this point of view, the agreement of normalized confinement indicated in Fig. 1 can be considered support for the applicability of plasma physics principles to tokamak transport, given the disparity in actual size, field, and density of the tokamaks involved. In future experiments, one should attempt to create flatter density profiles

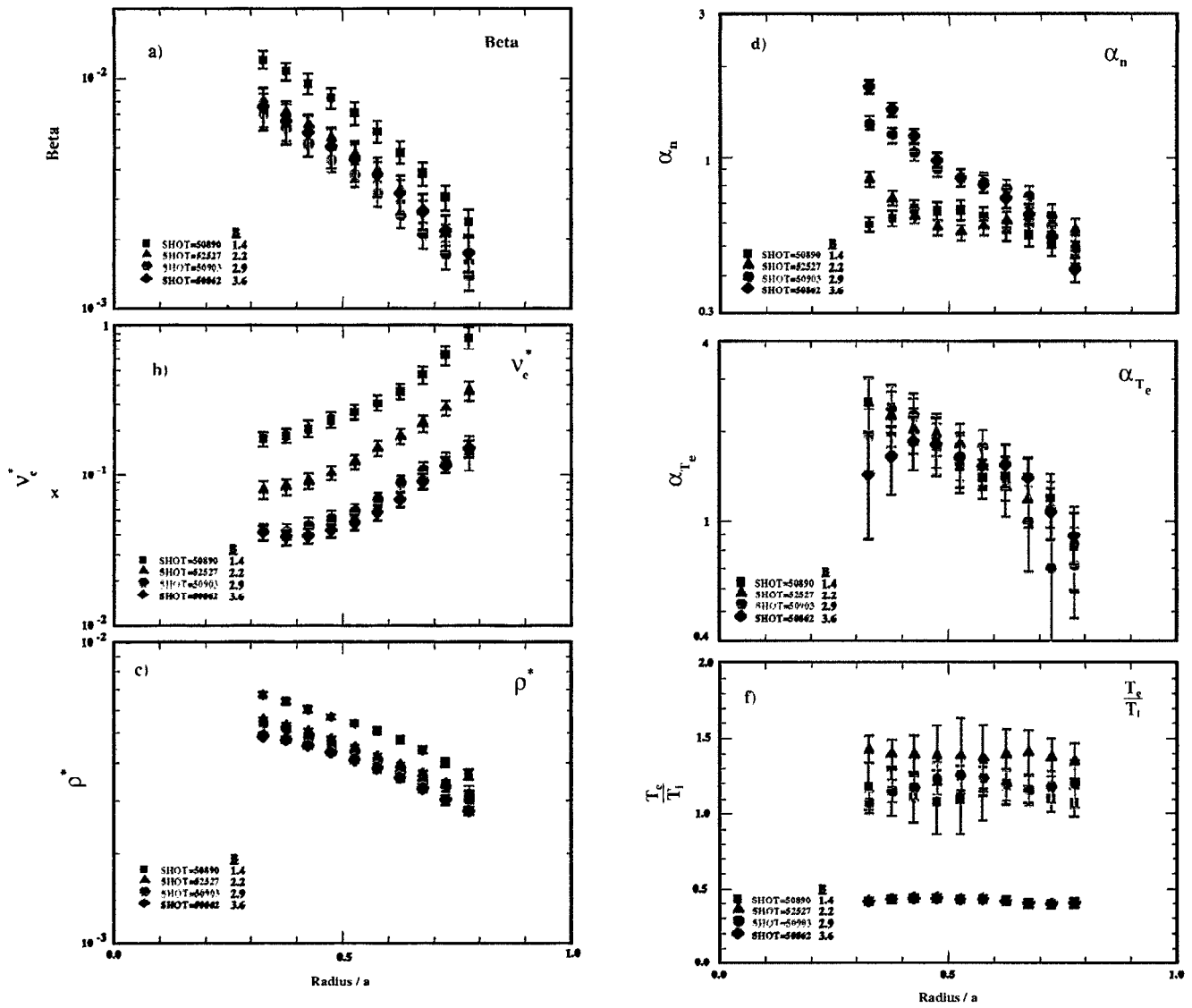


FIG. 15. Nondimensional parameter variation in the v^* scan. In the L-mode envelope ($r > 0.4$ m), nondimensional parameter variation is modest, but the low-magnetic-field member (shot=50890) has unintended higher values of ρ^* .

in what for TFTR are low-field, low-current, and low-density discharges.

IV. L-MODE GLOBAL CONFINEMENT SCALING

Empirical scaling relations⁴⁸ summarize how global confinement times vary as the parameters B_T , n_e , I_p , a , R , P , and κ that an experimentalist can control are varied. The latest efforts,⁴⁹ utilizing recent data from JET and TFTR in addition to data from older tokamaks, fit L-mode observations to within a rms error of $\approx 15\%$ over almost three orders of magnitude variation in confinement time. With modest changes, empirical scaling relations can be cast into a form that satisfies plasma physics principles⁵⁰ [see also Eqs. (39) and (40)]. How well do fits based on gyro-Bohm and Bohm scaling do in comparison? Can global confinement scaling data distinguish between Bohm and gyro-Bohm alternatives?

It is known^{12,51,52} that gyro-Bohm scaling gives a good account of the variation of tokamak global confinement data, the rms deviation being approximately $\pm 25\%$ over the same three orders of magnitude in confinement time. Indeed, one could argue that this combination of theoretical basis and observational agreement should make gyro-Bohm the preferred basis for extrapolating tokamak performance. Figure 3 portrays the latest ITER-P empirical scaling fit⁴⁹ and compares Bohm and gyro-Bohm formulas to global confinement data. The fit expressions are

$$\tau_{E,\text{gyro-Bohm}} = (0.31 \text{ sec}) \frac{I_{MA}^{0.8} a_m^{1.2} R_m^{1.0} n_{20}^{0.6}}{A^{0.2} P_{MW}^{0.6}}, \quad (16)$$

$$\tau_{E,\text{Bohm}} = (0.94 \text{ sec}) \frac{I_{MA}^{0.5} a_m^{2.3} R_m^{-0.3} n_{20}^{0.5}}{P_{MW}^{0.5}}, \quad (17)$$

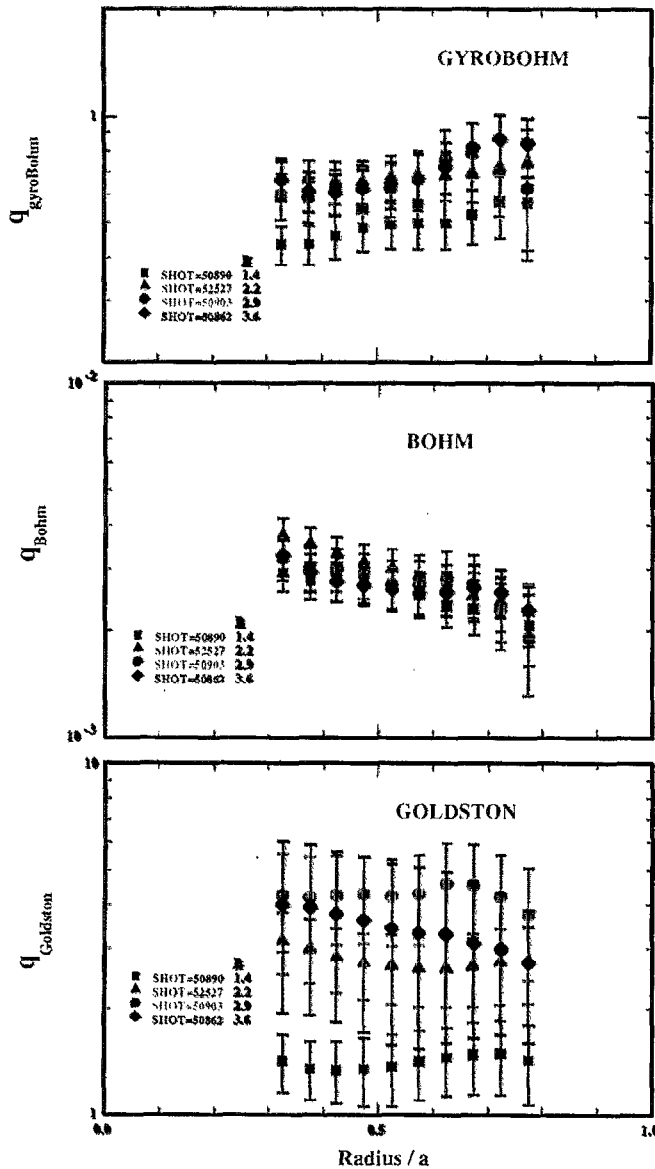


FIG. 16. Bohm-, gyro-Bohm-, and Goldston-normalized power flow for the v^* scan. If there were no unintended ρ^* variation, then the Bohm and gyro-Bohm curves would differ only by a factor of ρ^* given in Fig. 15(c). The good fit realized by Bohm normalization implies a very weak dependence of normalized power flow on collisionality v_e^* . Goldston-normalized power flow contains a $(v_e^*)^{-1/4}$ dependence not found in the data. See Eq. (30).

$$\tau_{E,ITER} = (0.048 \text{ sec}) \frac{A^{0.5} I_{MA}^{0.85} B_T^{0.2} n_{20}^{0.1} a_m^{0.3} R_m^{1.2} \kappa^{0.5}}{P_{MW}^{0.5}}. \quad (18)$$

Wherever the toroidal field appears in theoretical scalings (16) and (17), it has been replaced by I_p/a , which improves the fit. This is equivalent to permitting a scaling with the nondimensional parameter q_a . Free parameters in fits (16) and (17) are the exponent of (R/a) and the normalizing constant.

Both Bohm and gyro-Bohm global scaling relations fit the database well; they are virtually indistinguishable although they differ importantly in ρ^* scaling. One cannot

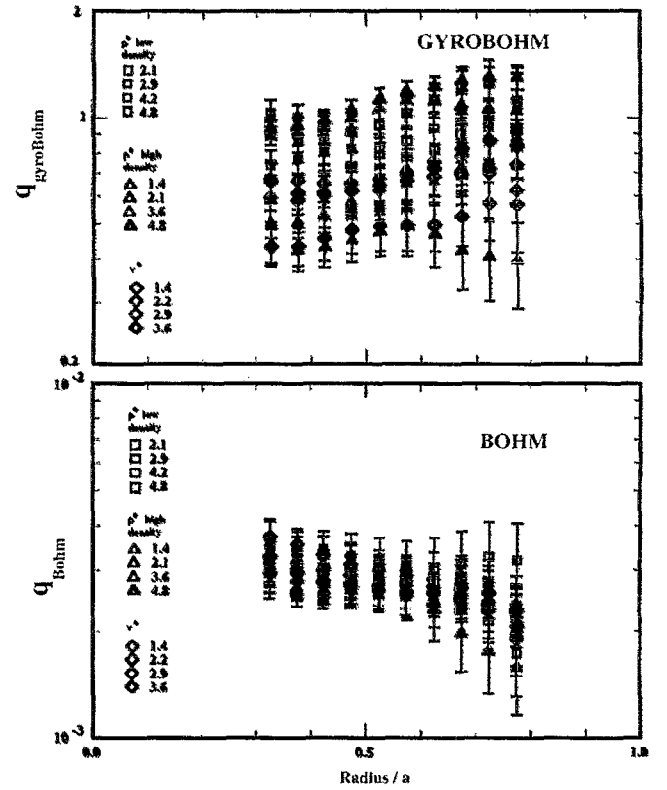


FIG. 17. Bohm and gyro-Bohm scaling for two ρ^* scans and one v^* scan (i.e., all shots listed in Table III).

determine which scaling would offer a more accurate extrapolation based on global confinement. Our Sec. VI and Table IV make clear that projections for ITER differ by a factor of ≈ 3 –5 in the $n_D(0)T_e(0)\tau_E$ product depending on whether a Bohm or gyro-Bohm scaling is used to extrapolate present experiments. The next section argues that one can distinguish between Bohm and gyro-Bohm scaling on the basis of a local heat flux comparison.

V. NONDIMENSIONAL SCALING OF L-MODE POWER FLOW ON TFTR

The goal of this section is to examine experimentally how L-mode transport scales with the nondimensional parameter ρ^* . We confine our attention to the region outside the sawtooth inversion radius, where there are no identifiable global transport processes. In this region, the thermal power flow through a magnetic surface, as inferred from beam power measurements and power deposition calculations, is cast into a nondimensional form via normalization by a power flow constructed from measured density, temperature, and magnetic field values to have Bohm (or gyro-Bohm) scaling. Thermal power flow is defined to be the power deposited inside a given magnetic surface to the thermal plasma by beams, Ohmic heating, and beam thermalization less charge exchange and radiative losses. Thus, the thermal power flow represents the sum of conductive and convective losses and includes all corrections for shine-through, orbit loss, and beam charge exchange. If Bohm

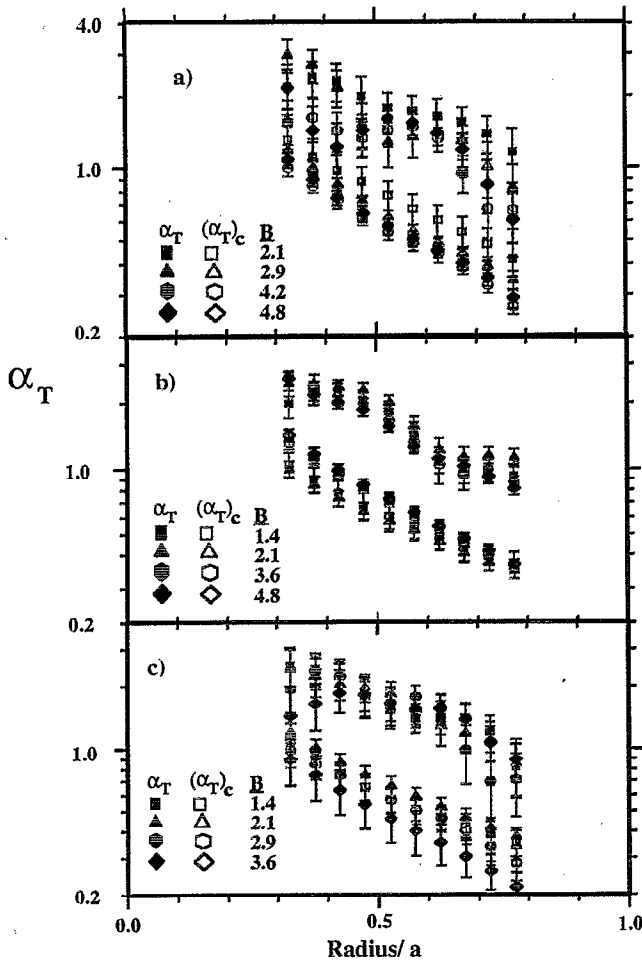


FIG. 18. Comparison between measured temperature gradients expressed as α_{Te} [see Eq. (3)] and the RLW critical temperature gradient, Eq. (32). (a) Low-density ρ^* scan, (b) high-density ρ^* scan, (c) ν^* scan.

scaling is correct, then the Bohm-normalized power flow should be a function of minor radius which remains invariant as ρ^* is varied from discharge to discharge.

To investigate the scaling of confinement in L-mode TFTR discharges with ρ^* , two sequences of discharges were created in which all nondimensional parameters, except for ρ^* , remained close to constant. The temperature and density of these discharges were adjusted to maintain constant effective collisionality ν_e^* and plasma β , according to the definitions:

$$\nu_e^* \equiv \frac{4\sqrt{2}\pi n_e Z_{\text{eff}} e^4 \ln \Lambda(qR)}{3T_e^2} \left(\frac{R}{r}\right)^{3/2}, \quad (19)$$

$$\beta \equiv \frac{8\pi n_e \{T_e + [(Z+1-Z_{\text{eff}})/Z]T_i\}}{B^2}, \quad (20)$$

where $Z \approx 6$ is the average charge of an impurity ion in TFTR. Let us assume that $T_e = T_i$ and combine (19) and (20) to express the relationship between density, temperature, and magnetic field intensity which must be realized so that β and ν_e^* remain invariant in two discharges. These relations are (ignoring impurity ion effects on β)

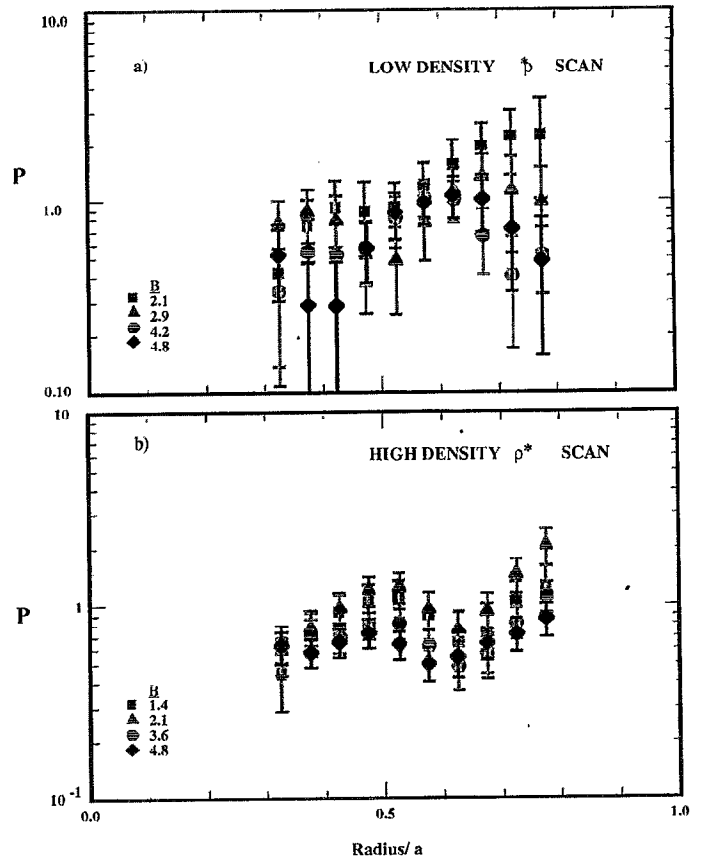


FIG. 19. Profile function P [see Eq. (34)] for (a) low-density ρ^* scan and (b) high-density ρ^* scan.

$$T_2 = T_1 \left(\frac{B_2}{B_1}\right)^{2/3} \left(\frac{a_2}{a_1}\right)^{1/3} \left(\frac{Z_{\text{eff},2}}{Z_{\text{eff},1}}\right)^{1/3} \left(\frac{\beta_2 \nu_1^*}{\beta_1 \nu_2^*}\right)^{1/3}, \quad (21)$$

$$n_2 = n_1 \left(\frac{B_2}{B_1}\right)^{4/3} \left(\frac{a_1}{a_2}\right)^{1/3} \left(\frac{Z_{\text{eff},1}}{Z_{\text{eff},2}}\right)^{1/3} \left(\frac{\nu_2^* \beta_2^2}{\nu_1^* \beta_1^2}\right)^{1/3}, \quad (22)$$

the factors involving β and ν^* being unity in an ideal ρ^* scan. If the discharges fulfill Eqs. (21) and (22), then the ratio of ρ^* is

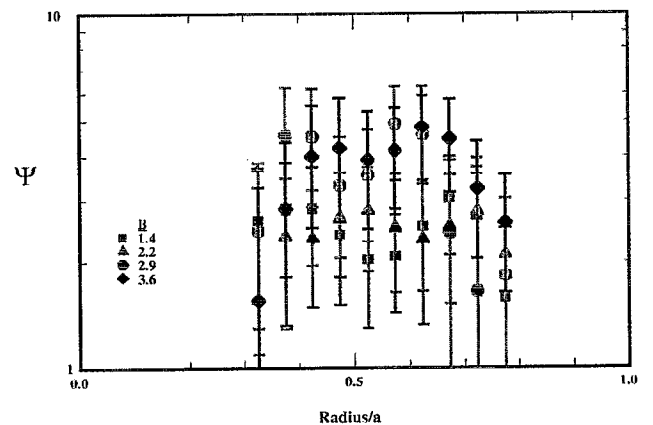


FIG. 20. Profile function $\Psi = P/\sqrt{\nu_e^*}$ for ν^* scan.

TABLE IV. Scaling from DIII-D and JET by a Bohm relation at constant v^* and β .

Quantity	Observed	DIII-D BPX ^a	ITER ^b	Observed	JET BPX ^a	ITER ^b
Shot	72220	22490
B (T)	2.1	9.0	4.85	2.8	9.0	4.85
R (m)	1.7	2.6	6.0	3.1	2.6	6.0
a (m)	0.62	0.79	21.15	1.0	0.79	2.15
I_p (MA) ^c	1.6	7.3	12.6	3.0	7.2	12.4
$n_D(0)$ (10^{20} m ⁻³)	0.85	5.5	1.7	0.8	4.1	1.30
τ_E , thermal(sec)	0.24	0.58	2.5	0.81	0.81	3.5
$T_i(0)$ (keV)	6.5	18.5	17.2	9.5	19.1	17.7
$T_e(0)$ (keV)	5.5	15.6	14.6	10.0	20.1	18.6
$n_D(0) T_i(0) \tau_E$	1.3	57	73	6.1	63	83
κ	2.1	2.1	2.1	1.9	1.9	1.9
Z_{eff}	1.2	1.2	1.2	1.3	1.3	1.3
β	0.041	0.041	0.041	0.012	0.012	0.012
Power (MW) ^d	9.1	142	192	7.5	38	52
ρ^* ratio	1.0	0.31	0.20	1.0	0.56	0.37

^aCapabilities with full upgrade.^bTechnology phase.^cScaled from data according to $I_p \propto B_T a^2 / R$.^dCombined thermonuclear and auxiliary power, $P - (dW/dt)$.

$$\rho_2^* = \rho_1^* \left(\frac{Z_{\text{eff},2}}{Z_{\text{eff},1}} \right)^{1/6} \left(\frac{B_1}{B_2} \right)^{2/3} \left(\frac{a_1}{a_2} \right)^{5/6} \left(\frac{\beta_2 v_1^*}{\beta_1 v_2^*} \right)^{1/6} \quad (23)$$

Two ρ^* scans were carried out, one at high density near the Marfe limit and one at lower density to vary the beam heating deposition and electron-ion temperature relaxation parameter. In our ρ^* scans, the minor radius a was fixed at $a=0.8$ m, Z_{eff} remained close to constant, and the toroidal field varied. Relatively low- q operation ($q=3.1$) was chosen, despite the large sawteeth, to make comparison more relevant to high-current reactors. Gas puffing was adjusted to obtain the density required by Eq. (22) and balanced neutral beam injection power was varied until Eq. (21) was satisfied. Satisfying both constraints was difficult due to a substantial beam fueling component, particularly with shot-to-shot changes in wall conditions leading to widely varying fueling efficiencies from gas puffing.

Table III gives parameters for two ρ^* scans at different β and v_e^* values as well as a v_e^* scan. Exact L-mode scaling was required in power to achieve the required β , i.e., $P \propto B^2$ as expressed in Eq. (26). Figures 4 and 5 show profiles for the ρ^* scans of n_e , T_e , and T_i on the equatorial plane. Electron density profiles from an eight-channel interferometer are shown. For the one-dimensional power flow analysis, the inverted interferometer density profile is symmetrized on computed magnetic surfaces to attain consistency with computed pressure profiles and magnetic measurements. Ion temperature profiles are from charge exchange spectroscopy (CHERS) observations using the 5292 Å line of C⁵⁺. Figures 6 and 7 show the time evolution of $T_e(0)$, n_e , NBI power, and diamagnetic stored energy. There is no T_e data from electron cyclotron emission (ECE) data for the two low-field cases. The Thomson scattering and CHERS measurement times are shown. In the case of the high-power shots 52504 and 56311, there are two operating

neutral beam lines which cross the CHERS sightline at different angles during most of the heating period. Just before the CHERS time, one beam line is switched off to avoid delocalization of the measurement. Figure 8 presents ECE electron temperature profile observations of a representative discharge. These observations show the sawtooth inversion radius to be $r \approx 0.24$ m and indicate that temperature profiles (and hence transport) are negligibly affected by sawteeth for $r/a > 0.3$. This holds true for all our discharges since they have the same q value.

Next, we must examine whether nondimensional parameters remained close to constant. Our objective is to have the parameters v_e^* , β , T_e/T_i , and q as well as the profile shape parameters α_T and α_n [see Eq. (3)] constant throughout the range of minor radius $0.3 < r/a < 0.8$ which is free of sawtooth effects and where the temperatures can be measured with sufficient accuracy. Figures 9 and 10 attest to our success and also indicate potential sources of error. Agreement of v_e^* and β is sufficiently good that the factors involving v_e^* and β in Eqs. (24)–(26) remain close to unity. Similarly the shape profiles are in adequate agreement, although lower field discharges had somewhat more peaked density profiles (i.e., higher α_n).

The error bars in Fig. 9 and subsequent figures represent the standard deviation of an ensemble of 150 profiles, each generated by adding to the measured profile quantities (e.g., n_e, T_e) an amount chosen randomly from a Gaussian distribution whose standard deviation is equal to the estimated random experimental error. Every profile so generated was smoothed by a triangular weighting function of full width 10 cm at half-maximum. This reduces the error associated with data that have several independent observations within 10 cm—essentially only the Thomson scatter T_e data. Because our interest is in systematic trends, the

error bars do not include an estimate of errors that are common to all members of a scan.

L-mode plasmas are distinguished from supershot plasmas^{9,53} in that $T_i/T_e \approx 1$ for L mode. The existence of supershot plasmas, where transport does not degrade with increasing T_i , suggests that T_i/T_e is an important nondimensional parameter in confinement physics. The concern is that, if equilibration does not assure $T_e \approx T_i$, then one cannot rigorously distinguish between a systematic variation of power flux with ρ^* or with T_e/T_i . Even in our high-density ρ^* scan, the equilibration parameter $\langle v_{ie} \rangle \tau_E \propto (\nu^*/\rho^*)$ had values $\langle v_{ie} \rangle \tau_E \approx 1$, which are not sufficient to assure T_e/T_i remains independent of ρ^* . Fortunately, a large systematic variation in T_e/T_i did not occur as ρ^* changed in the high-density ρ^* scan [Fig. 10(f)]. In the low-density ρ^* scan, the T_e/T_i profiles again showed minimal systematic variation except for the low-field member where low- T_i values resulted in high values of T_e/T_i [Fig. 9(f)].

A source of systematic error arises in the ion temperature measurements of high-density discharges. CHERS measurements exploit emission from hydrogenic impurity ions after charge exchange with beam neutrals and are assumed to be local, with emitted light coming from the sightline-neutral beam intersection volume. However, light arising from electron impact excitation of the product C^{+5} ions can contribute to the spectrum.⁵⁴ This is called the plume effect. The CHERS sightlines view a co-injecting neutral beam in the midplane and their tangency radii are near the neutral beam-sightline intersection radii. For this sightline-neutral beam geometry, the plume emission comes from cooler regions of the plasma than the prompt emission, potentially adding a cold component to the observed spectrum. The ratio of plume emission to prompt emission is expected to be highest in high-density plasmas, where beam attenuation is strongest and prompt emission correspondingly diminished. The impact of this issue on these experiments is being addressed both by modeling and measurements. Preliminary modeling of the spectrum including both prompt and plume emission, indicates that the central ion temperature in the plasmas with the highest line-averaged electron density (shot 56311) may be 500–800 eV higher than reported in Fig. 5, bringing it closer to the central electron temperature. Ion temperatures outside of the sawtooth region should be elevated by up to 300 eV for this shot, bringing T_i and T_e within 100–200 eV of each other. The effect of the plume on T_i measurements of other plasmas is somewhat smaller for the high-density plasmas and completely negligible in the lowest density plasmas. The predicted ratio of plume emission to prompt emission after charge exchange has been found to be in good agreement with plume measurements made in other L-mode plasmas, giving confidence that the corrections to the measured T_i are reliable.

The ion temperatures given in Figs. 4, 5, and 14 have not been corrected for plume effects and should be increased as discussed above. Ion temperature uncertainties arising from instrumental profiles widths and background light subtraction are negligible.

During the course of a ρ^* scan, the calculated NBI power deposition profile varies as illustrated in Fig. 11. Consequently, the appropriate scaling comparisons must involve a local nondimensional power flow, rather than a global energy confinement time. Note that, according to Fig. 11, the power deposition fraction varies appreciably in the region $0.4 \text{ m} < r < 0.7 \text{ m}$, and this variation must enter any local transport analysis. Radiative loss is negligible in the bulk plasma. Since our interest is in thermal confinement, we compare power flows to expressions containing temperature and density, thereby avoiding the complication of fast particle energy content inherent in global τ_E values based on magnetic energy observations. Comparisons are to expressions for the power flow with three different scaling properties: Bohm [Eq. (4)], gyro-Bohm [Eq. (2)], and an expression with the density and temperature required for local power flow to exhibit the empirical Goldston–Aachen⁵⁵ scaling when the device size remains fixed. Although Goldston–Aachen scaling is effectively consistent with the plasma physics principles discussed in Sec. III, its functional form does not rest on a first-principles derivation. The nondimensional power flows are

$$q_{\text{Bohm}} = \frac{Q(r)eB}{32\pi^2 n_e T_e^2 c a} \left[\frac{(a^2 - r^2)^2}{r^3 R} \right] \propto \frac{Q(r)(\nu^*)^{1/3}}{B^{5/3} a^{4/3} Z_{\text{eff}}^{1/3} \beta^{4/3}}, \quad (24)$$

$$q_{\text{gyro-Bohm}} = \frac{Q(r)e^2 B^2}{32\pi^2 \sqrt{2} n_e T_e^{5/2} M_i^{1/2} c^2} \left[\frac{(a^2 - r^2)^2}{r^3 R} \right] \propto \frac{Q(r)(\nu^*)^{1/2}}{B(Z_{\text{eff}} a)^{1/2} \beta^{3/2}}, \quad (25)$$

$$q_{\text{Goldston}} = (\text{const}) \frac{Q(r)B}{n^2 T_e^2} \left[\frac{(a^2 - r^2)^2}{r^3 R} \right] \propto \frac{Q(r)}{B^2 \beta^2}. \quad (26)$$

Rigorously, the nondimensional factor in [] brackets should be regarded as an empirical factor chosen to account for most of the minor radius variation of $Q(r)$ not included in n_e and T_e . The rationale for the choice of this factor is that it would result from Eq. (1) if α_n and α_T were constant. Our results indicate that this *ad hoc* geometric factor does eliminate most of the minor radius dependence, improving the clarity of the graphical display of our results. However, in all our results one really is comparing nondimensional power flows for various members of the scans at fixed minor radius.

Let us note that our procedure is identical to comparing nondimensional thermal diffusivities, provided α_T does not vary among members of the scan. Figures 9(e) and 10(e) show α_T to be quite constant. Our comparison avoids the use of numerical derivatives of experimental data. The right-hand forms of Eqs. (24)–(26) indicate how deviations in β , ν^* , and Z_{eff} from an ideal ρ^* scan will affect our determination of the various q 's. The ν^* and β exponents are not large and Figs. 9 and 10 indicate that errors in matching ν^* and β are small compared to the factor ρ^* which separates the members of the scan.

Figures 12 and 13 constitute the principal results of this paper. They show that local power flux is better fit by

a Bohm rather than a gyro-Bohm normalization. The local power flow normalized by Goldston–Aachen global scaling is also not successful. The definitiveness of this conclusion is tempered by the fact that just the ρ^* ratio (only a factor of 2 from Table III) separates Bohm from gyro-Bohm scaling, by the difficulties in measuring T_e , and by systematic variation of α_n across the scan. The α_n variation portrayed in Figs. 9(d) and 10(d) is in the sense that lower density discharges tend to have higher α_n . Qualitatively, one expects steeper density profiles (higher α_n) to correspond to greater power flow—a trend corroborated by H-mode observations of better core confinement with flatter density profiles. Such a qualitative trend would imply that discharges with flatter density profiles should have even lower power flow and would increase discrepancy between experiment and gyro-Bohm scaling. But steeper density profiles can also decrease power flux, as supershot observations show.^{9,53} Since our scans have rather flat profiles and operate in high recycling conditions, we argue that they are closer to H-mode, rather than to supershot, confinement physics. Thus the systematic trend in α_n strengthens the argument for Bohm scaling.

An interesting observation is that, if gyro-Bohm scaling governed transport, then a toroidal field scan of Ohmic discharges where the density varied according to Eq. (22), will automatically produce a temperature scan fulfilling Eq. (21). For example, fine-scale dissipative-trapped-electron modes yield the scaling $T_e \propto (B^2 a Z_{\text{eff}})^{1/3}$ and are often invoked to explain neo-Alcator scaling.⁵¹ We attempted such an Ohmic toroidal field scan in TFTR at low density in the linear Ohmic regime where neo-Alcator scaling holds. Unfortunately, in a graphite limiter machine, Z_{eff} cannot be effectively controlled and it varied systematically ($4.6 < Z_{\text{eff}} < 6.8$), so that v_e^* also varied systematically. Even so, Bohm normalization of power flux again proved superior to gyro-Bohm, but Goldston normalization was marginally better than Bohm. Since these plasmas had $T_e \gg T_i$, they are not representative of fusion reactor plasmas.

One can also inquire: How does transport depend on collisionality? From a nondimensional point of view, one can answer this question by creating a series of discharges in which ρ^* and β (as well as nondimensional profiles) remain fixed, but v_e^* varies. This requires the temperatures, densities, and magnetic fields of two discharges to be related via

$$n_2 = n_1 (a_1^2 / a_2^2), \quad (27)$$

$$T_2 = T_1 (B_2 a_2 / B_1 a_1)^2. \quad (28)$$

The variation of v_e^* is then

$$(v_e^*)_2 = (v_e^*)_1 \left(\frac{B_1}{B_2} \right)^4 \left(\frac{a_1}{a_2} \right)^5 \left(\frac{Z_{\text{eff},2}}{Z_{\text{eff},1}} \right). \quad (29)$$

Table III lists parameters of shots entering the v_e^* scan. At the high-field, high-power end, these discharges had supershot cores ($r < 0.25$ m) surrounded by L-mode-like envelopes. Figure 14 shows the profile data for this scan. Our interest centers on transport in the L-mode envelope. Fig-

ure 15 portrays the variation in nondimensional parameters. Except for the lowest density member, which had a somewhat too high electron temperature (and hence too large a value for ρ^*), most nondimensional parameters remained close to constant. The exceptions are Z_{eff} and T_e/T_i . The increase of Z_{eff} with B simply reduces the range of v_e^* variation with B across the scan.

Figure 16 plots the Bohm-, gyro-Bohm-, and Goldston-normalized power flows. Our first conclusion is that normalized power flow is independent of v_e^* as theory would suggest for collisionless plasmas. Second, Bohm scaling again accounts for the variation of power flow with the (unintended) variation of ρ^* . The ambiguity introduced by T_e/T_i variation is that our observations are also consistent with transport that decreases as v_e^* decreases and increases as T_e/T_i decreases. Because minor radius remains constant throughout the scan, one can relate Goldston-normalized power flow to Bohm-normalized power flow via

$$q_{\text{Goldston}} \propto q_{\text{Bohm}} \left(\frac{Ba}{n_e} \right) \propto q_{\text{Bohm}} \left(\frac{\rho^* Z_{\text{eff}}}{v_e^* \beta^3} \right)^{1/4} a^{7/4}. \quad (30)$$

Although the predicted collisionality variation is weak—only $(v_e^*)^{-1/4}$ —Fig. 16 shows that Bohm normalization collapses the data better than Goldston normalization. Thus, a Goldston scaling for power flow implies a variation with v_e^* (at constant ρ^* , β , and a) not exhibited in the data.

Indeed, Bohm-normalized power flow collapses power flow data from all our scans into a single curve. Figure 17 shows that data from all scans (ρ^* and v_e^*) listed in Table III, normalized according to Eq. (24), can be adequately represented by the empirical, but extraordinary simple, formula

$$q_{\text{Bohm}} = (0.004 \pm 0.001) \exp[-0.7(r/a)]. \quad (31)$$

In other words, increasing the toroidal field and current in TFTR clearly does not result in the improved confinement that a gyro-Bohm theory would require. By contrast, Bohm scaling predicts $\tau_E \propto B^{1/3}$, which combines with the power deposition changes in Fig. 11 to yield $\tau_E \approx \text{const}$ in accord with the data of Table III.

L-mode confinement on JET has been successfully modeled with the Rebut–Lallia–Watkins (RLW) empirical, critical-temperature-gradient diffusivity model.⁵⁶ It is interesting to recast the RLW model in terms of our nondimensional parameters and ask whether the nondimensional scaling properties of TFTR L-mode data are in accord with those of the RLW model. Let us first express the RLW critical temperature gradient in terms of a critical value of α_T ,

$$\begin{aligned} (\alpha_T)_c &= \frac{(a^2 - r^2)}{2rT_e} \left| \frac{dT_e}{dr} \right|_c \\ &= 0.12 \left(\frac{a^2 - r^2}{r^{1/4} R^{7/4}} \right) \frac{\sqrt{v_e^*}}{q^{3/2} \beta} \left(\frac{|j| R \mu_0}{2B_T} \right)^{1/2} \left(\frac{2\eta_{\parallel} nc}{\eta_{\parallel} mx} \right)^{1/2}, \end{aligned} \quad (32)$$

where the current density j is normalized to the current density associated with $q(0)=1$ in a circular tokamak and the resistivity ratio uses the notation and formulas of Zarnstorff.⁵⁷ Note that $(\alpha_T)_c$ is independent of ρ^* and thus should remain fixed in a ρ^* scan but should vary in a ν^* scan. Figure 18 presents measured values of α_T and values of $(\alpha_T)_c$ computed from experimental n_e and T_e profiles. The current density j is derived from the loop voltage and neoclassical resistivity and includes small bootstrap and beam-driven contributions. Throughout most of the discharge, observed temperature gradients are large compared to the critical gradient, placing TFTR L modes in the regime governed by anomalous conductivity according to the RLW model. When electron and ion temperatures are equal, the anomalous RLW power flow across a magnetic surface simplifies to

$$Q_{RLW}(r) = Q_{gB} H \left(1 - \frac{(\alpha_T)_c}{|\alpha_T|} \right) H(s) P \left(\frac{r}{a} \right). \quad (33)$$

Here P is a profile function

$$P = \frac{(2.43)}{s} \left(\frac{r}{R} \right)^{7/4} \sqrt{\frac{\nu_e^* \alpha}{\beta \ln \Lambda}} \left(1 - \sqrt{\frac{r}{R}} \right) (\sqrt{1 + Z_{eff}} + 2) \\ \times (\alpha_T + 2\alpha_n) [\alpha_T - (\alpha_T)_c] \quad (34)$$

and Q_{gB} is the gyro-Bohm power flow used for normalization in (25)

$$Q_{gB} = \frac{32 \sqrt{2} \pi^2 n_e T_e^{5/2} M_i^{1/2}}{e^3 B^2} \left[\frac{r^3 R}{(a^2 - r^2)^2} \right]. \quad (35)$$

The profile function P is also independent of ρ^* and is plotted in Fig. 19 for our ρ^* scans. For the low-density ρ^* scan, the systematic trend is for higher P at lower ρ^* , arising principally from steeper density gradients α_n [Fig. 9(d)]. For the high-density ρ^* scan, P is independent of ρ^* . It follows from the RLW model that the gyro-Bohm normalized power flow should have the same systematic trend with ρ^* as the function P . In contrast, Figs. 12(a) and 13(a) show the gyro-Bohm normalized power flow systematically increasing with decreasing ρ^* —in contrast to the systematic trends of Fig. 19. In brief, Figs. 12(a) and 13(a) show that TFTR data do not display the confinement improvement with decreasing ρ^* expected from gyro-Bohm scaling and indicate that Bohm scaling is to be preferred over RLW scaling.

The RLW model has an explicit collisionality scaling

$$Q_{RLW}(r) = Q_{gB} \sqrt{\nu_e^*} \Psi, \quad (36)$$

where Ψ is a profile function independent of ρ^*

$$\Psi = P / \sqrt{\nu_e^*}. \quad (37)$$

Collisionality enters Ψ only through $(\alpha_T)_c \propto \sqrt{\nu_e^*}$. Thus when $\alpha_T \gg (\alpha_T)_c$, as is the case for most values of the minor radius [see Fig. 18(c)], gyro-Bohm-normalized power flow should increase with collisionality according to the RLW model. Figure 20 shows that Ψ is indeed independent of ν^* within rather large errors arising from differentiating ex-

perimental data. In contrast to the predicted proportionality to $\sqrt{\nu_e^*}$, Fig. 16 shows that gyro-Bohm normalized power flow has either a weak or an inverse dependence on collisionality.

While ρ^* and $\sqrt{\nu_e^*}$ vary only by a factor of 2 in our scans, the error bounds on our data are sufficient to conclude that TFTR confinement is not following the ρ^* scaling implied by the RLW model. The large error bars on Ψ preclude a definitive conclusion regarding ν_e^* scaling. Nonetheless, transport appears independent of collisionality.

Since RLW is a gyro-Bohm scaling, the $nT\tau_E$ values extrapolated to ITER from JET and DIII-D via RLW scaling are the Bohm values reported in Table IV divided by the ρ^* ratio. A very favorable ignition margin—close to 4 for the JET extrapolation—results. Let us note that RLW scaling produces a power loss proportional to \sqrt{R} when the major radius dependence of ν^* is included in (34) and consequently modestly favors high-aspect-ratio designs. Our experiments do not address aspect-ratio scaling.

VI. DISCUSSION

Our principal findings are that local confinement in TFTR exhibits a Bohm-like scaling when collisionality and β are held nearly fixed and that the measured Bohm-normalized power flow does not depend on collisionality. The difference between local Bohm scaling of power flow and L-mode (i.e., Goldston) global scaling arises because of variations in the power deposition profile (Fig. 11). Arguments presented in Sec. II imply that Bohm scaling arises from long-wavelength fluctuations that scale according to the system size. Theoretically, trapped-ion modes¹³⁻¹⁶ have this property and our results suggest renewed attention to modes with frequencies comparable to or below the ion bounce frequency. One should note that the ion bounce frequency in TFTR is low,

$$\nu_b = \left(\frac{T_i}{M_i} \right)^{1/2} \frac{1}{2\pi q R} \left(\frac{r}{R} \right)^{1/2} \approx 2.5 \text{ kHz} \left(\frac{T_i}{1 \text{ keV}} \right)^{1/2}, \quad (38)$$

so that observed mode frequencies will likely be dominated by the Doppler shift arising from toroidal rotation. Furthermore, since trapped-ion modes have $k_\perp \rho_s \ll 0.1$, their direct observation by laser/microwave scatter methods has not been possible. Recently, the new technique of beam emission spectroscopy¹⁸ has shown that fluctuations in the range $0 < k_\perp < 1.5 \text{ cm}^{-1}$ exist at the $\tilde{n}/n \approx 0.005$ level and have frequencies up to 20 kHz. To within measurement uncertainties, the frequency is simply that arising from toroidal rotation. In the plasma frame, the frequencies lie below 5 kHz, and hence in the trapped-ion regime.

A clear prediction exists: Bohm scaling implies that the amplitude of long-wavelength fluctuations should be independent of ρ^* in a scan similar to the ones reported here. If gyro-Bohm scaling prevailed, then, at fixed wavelength, fluctuations on the long-wavelength side of the side spectral peak should decrease with decreasing ρ^* .

Bohm scaling is consistent with ITER-P scaling of global confinement because ITER-P scaling, when represented as a diffusivity, is almost identical to a Bohm thermal diffusivity with additional β and ν_e^* dependences. Indeed, the diffusivity formula

$$\chi = \frac{T_e \mathcal{L}}{eB} (\beta^2 \nu_e^*)^{1/4} f(q, r/R, \kappa, \dots) \quad (39)$$

yields a confinement time consistent with

$$\tau_E \propto I_p R^{1.375} n^{0.125} P^{-0.50}. \quad (40)$$

The exponents in (40) are almost precisely those of (18). Of course, such simple arguments cannot determine scaling with R/a , q^* , κ , etc. Formula (39) is consistent with our finding of Bohm scaling in ρ^* and little dependence on ν_e^* . Our results of Bohm scaling with weak dependence on collisionality contrast with the trapped-ion-mode diffusivity expressions derived by Biglari and Diamond,¹³ which scale according to gyro-Bohm with an additional inverse dependence on collisionality. Fits to the global database,⁵⁰ constrained by plasma physics principles, find a scaling with ρ^* even stronger than gyro-Bohm and clearly at variance with our local analysis.

To what extent do TFTR data favor a diffusivity independent of collisionality? From Fig. 15(b), one determines that ν_e^* varied by a factor of 5 in our scan and a factor of $(5)^{1/4} = 1.5$ lies at the limits of the error bars in Fig. 16(b). In view of the variations in α_n and T_e/T_i in Figs. 15(d) and 15(f), we cannot unequivocally determine the exponent of ν_e^* in (39) to within ± 0.25 ; power flow could well depend on α_n and T_e/T_i . Nonetheless, Goldston normalization [Fig. 16(c)] effectively has the $(\nu_e^*)^{1/4}$ effect. [See Eq. (30).] Comparing Figs. 16(b) and 16(c), we conclude that TFTR data are more consistent with simple Bohm scaling than with an additional factor of $(\nu_e^*)^{1/4}$.

Future experiments are needed to investigate the β scaling suggested by (39). If the $\sqrt{\beta}$ scaling is supported by a β -scan experiment, it would indicate that electromagnetic effects are essential to the tokamak transport mechanism. Theoretical work should be accordingly revised. Since the $\sqrt{\beta}$ factor is responsible for half the value of the plasma current scaling exponent in (39), it plays an important role in projecting tokamak performance. The analysis of Christiansen *et al.*⁵⁰ finds even stronger β scaling.

Bohm scaling further implies that confinement will not depend on the hydrogen isotope. Indeed, recent TFTR observations find a minimal isotope effect—less than 20% variation in τ_E from proton to deuterium plasmas for L-mode discharges.⁵⁸ This is in accord with data from DIII-D⁵⁹ and JET.⁶⁰ The trend of the TFTR data⁶¹ is opposite to the prediction of gyro-Bohm scaling: a small but measurable increase in the confinement of deuterium plasmas relative to proton plasmas is observed.

What does Bohm scaling predict regarding the performance of future devices, such as the Burning Plasma Experiment²² and ITER (Technology Phase)?²³ Let us scale at constant ν_e^* and β from two H-mode discharges in shaped tokamaks notable for their high $n_D(0)T_i(0)\tau_E$ values. The extrapolation is at constant aspect ratio. Table IV

gives the results. BPX is projected to meet a goal of $Q \gg 5$. Ignition requires $n_D(0)T_i(0)\tau_E \geq 60$ and ITER just does attain it under Bohm scaling. Gyro-Bohm extrapolations for τ_E and $n_D(0)T_i(0)\tau_E$ would be more favorable by a factor of the inverse ρ^* ratio, which has a large value ($1/\rho^*$ ratio ≈ 3 – 5) for ITER. We noted in Eqs. (32)–(37) that Rebut–Lallia–Watkins scaling is a particular case of gyro-Bohm scaling.

These projections rest, of course, on the supposition that H-mode confinement has the same Bohm scaling as the L-mode plasmas investigated in this paper. A comparison⁶² of DIII-D and JET discharges support this supposition. H-mode confinement at fixed B_T in these two tokamaks can be summarized by the empirical formula (which assumes a $n_e^{0.0}$ dependence)

$$\tau_E \propto I_p^{1.03 \pm 0.07} P^{-0.46 \pm 0.06} L^{1.48 \pm 0.09} n_e^{0.0}, \quad (41)$$

where L denotes plasma size at fixed aspect ratio. This formula is very close to scaling relation (40) which results from a diffusivity with a Bohm scaling in ρ^* . The DIII-D–JET comparison complements our TFTR experiments in that the ρ^* variation results from a minor radius variation at fixed B_T instead of vice versa. Although the JET–DIII-D comparison did not attempt to identify and compare discharges with identical ν_e^* and β values, scans which independently vary four quantities—minor radius, currents, power, and density—suffice to determine scaling properties with ρ^* , ν_e^* , β , and q provided plasma physics principles govern confinement.

Experimentally, our work points out how difficult it is to create discharges with all nondimensional parameters constant, except for ρ^* . In more conventional confinement scans, several nondimensional parameters may vary simultaneously and it becomes difficult to discern the true scaling of confinement. Careful attention to potential and actual covariations of nondimensional parameters, in particular power deposition profile, appears essential to elucidating the mechanism controlling energy confinement in tokamaks.⁶³

ACKNOWLEDGMENTS

We thank S. Wolfe for Alcator-C data and S. Kaye for Fig. 3. This work benefited from discussions with R. Hawryluk, S. Kaye, E. Mazzucato, K. McGuire, S. Paul, W. Tang, and S. Zweben. We especially thank R. Goldston and R. Waltz for encouraging and supporting this experiment. One of us (C.W.B.) thanks D. Meade and K. Young for supporting his stay at the Princeton Plasma Physics Laboratory.

This work was supported by U.S. Department of Energy Contract No. DE-AC02-76-CHO3073.

¹W. M. Tang, Nucl. Fusion **18**, 1089 (1978); P. C. Liewer, *ibid.* **25**, 543 (1985); F. Romanelli, Plasma Phys. Controlled Fusion **31**, 1535 (1989).

²A. J. Wootton, B. A. Carreras, M. Matsumoto, K. McGuire, W. A. Peebles, Ch. P. Ritz, P. W. Terry, and S. J. Zweben, Phys. Fluids **B 2**, 2879 (1990).

³R. T. Snider, Nucl. Fusion **30**, 2400 (1990).

⁴T. Ozeki, M. S. Chu, L. L. Lao, T. S. Taylor, M. S. Chance, S. Kinosh-

- ita, K. H. Burrell, and R. D. Stambaugh, *Nucl. Fusion* **30**, 1425 (1990); H. Zohm, F. Wagner, M. Endler, J. Gernhardt, E. Holzhauser, W. Kerner, and V. Mertens, *ibid.* **32**, 489 (1992).
- ⁵P. W. Terry, J.-N. Lebouef, P. M. Diamond, D. R. Thayer, J. E. Sedlak, and G. S. Lee, *Phys. Fluids* **31**, 2920 (1988).
- ⁶H. Biglari, P. H. Diamond, M. N. Rosenbluth, *Phys. Fluids B* **1**, 109 (1989).
- ⁷R. R. Dominguez and R. E. Waltz, *Phys. Fluids* **31**, 3147 (1988).
- ⁸T. S. Hahm and W. M. Tang, *Phys. Fluids B* **1**, 1185 (1989).
- ⁹D. M. Meade, V. Arunasalam, C. W. Barnes, M. G. Bell, R. Bell, M. Bitter, R. Boivin, N. L. Bretz, R. Budny, C. E. Bush, A. Cavallo, C. Z. Cheng, T. K. Chu, S. A. Cohen, S. Cowley, S. L. Davis, D. L. Dimock, J. Dooling, H. F. Dylla, P. C. Efthimion, A. B. Ehrhardt, R. J. Fonck, E. D. Fredrickson, H. P. Furth, R. J. Goldston, G. J. Green, B. Grek, L. R. Grisham, G. W. Hammett, R. J. Hawryluk, K. W. Hill, J. C. Hosea, R. B. Howell, H. Hsuan, R. A. Hulse, A. C. Janos, D. L. Jassby, F. C. Jobs, D. W. Johnson, L. C. Johnson, R. Kaita, S. M. Kaye, J. Kesner, C. Kieras-Phillips, S. J. Kilpatrick, H. Kugel, P. H. LaMarche, B. LeBlanc, D. M. Manos, D. K. Mansfield, E. S. Marmar, M. E. Mauel, E. Mazzucato, M. P. McCarthy, D. C. McCune, K. M. McGuire, S. S. Medley, D. R. Mikkelsen, D. A. Monticello, R. W. Motley, D. Mueller, J. Murphy, Y. Nagayama, G. A. Navratil, R. Nazikian, D. K. Owens, H. K. Park, W. Park, S. F. Paul, R. Perkins, S. Pitcher, A. T. Ramsey, M. H. Redi, G. Rewoldt, D. R. Roberts, A. L. Roquemore, P. H. Rutherford, S. A. Sabbagh, G. Schilling, J. Schivell, G. L. Schmidt, S. D. Scott, J. Snipes, J. E. Stevens, W. Stodiek, B. C. Stratton, E. J. Synakowski, W. M. Tang, G. Taylor, J. L. Terry, J. R. Timberlake, H. H. Towner, M. Ulrickson, S. von Goeler, R. M. Wieland, M. Williams, J. R. Wilson, K. L. Wong, M. Yamada, S. Yoshikawa, K. M. Young, M. C. Zarnstorff, and S. J. Zweben, in *Plasma Physics Controlled Nuclear Fusion Research, 1990*, Proceedings of the Thirteenth International Conference, Washington, D.C. (International Atomic Energy Agency, Vienna, 1991), Vol. 1, p. 9.
- ¹⁰M. C. Zarnstorff, C. W. Barnes, P. C. Efthimion, G. W. Hammett, W. Horton, R. A. Hulse, D. K. Mansfield, E. S. Marmar, K. McGuire, G. Rewoldt, B. C. Stratton, R. J. Synakowski, W. Tang, J. Terry, X. Q. Xu, M. G. Bell, M. Bitter, N. L. Bretz, R. Budny, C. E. Bush, R. J. Fonck, E. D. Fredrickson, H. P. Furth, R. J. Goldston, B. Grek, R. J. Hawryluk, K. W. Hill, H. Hsuan, D. W. Johnson, D. C. McCune, D. M. Meade, D. Mueller, D. K. Owens, H. K. Park, A. T. Ramsey, M. N. Rosenbluth, J. Schivell, G. L. Schmidt, S. D. Scott, G. Taylor, and R. M. Wieland, in Ref. 9, p. 109.
- ¹¹B. B. Kadomstev, *Sov. J. Plasma Phys.* **1**, 295 (1975).
- ¹²See National Technical Information Service Document No. DE 90014821 ("Issues in Tokamak/Stellarator Transport and Confinement Enhancement Mechanisms," Princeton Plasma Physics Laboratory Report PPPL-2708, 1990, by F. W. Perkins). Copies may be ordered from the National Technical Information Service, Springfield, Virginia 22161.
- ¹³P. H. Diamond and H. Biglari, *Phys. Rev. Lett.* **65**, 2865 (1990); H. Biglari and P. H. Diamond, *Phys. Fluids B* **3**, 1797 (1991).
- ¹⁴R. Marchand, W. M. Tang, and G. Rewoldt, *Phys. Fluids* **23**, 1164 (1980).
- ¹⁵W. Tang and G. Rewoldt (private communication, 1992).
- ¹⁶N. T. Gladd and D. W. Ross, *Phys. Fluids* **16**, 1706 (1973).
- ¹⁷N. Bretz, R. Nazikian, and K. L. Wong, *Proceedings 17th European Conference Controlled Fusion and Plasma Physics*, Amsterdam, 1990 (European Physical Society, Amsterdam, 1990), Vol. 4, p. 1544; T. Crowley and E. Mazzucato, *Nucl. Fusion* **25**, 507 (1985).
- ¹⁸R. J. Fonck, S. F. Paul, D. R. Roberts, Y. J. Kim, N. Bretz, D. Johnson, R. Nazikian, and G. Taylor, *Proceedings 18th European Conference Controlled Fusion and Plasma Physics*, Berlin, 1991 (European Physical Society, Amsterdam, 1991), Vol. 1, p. 269.
- ¹⁹R. E. Waltz, R. R. Dominguez, and F. W. Perkins, *Nucl. Fusion* **29**, 351 (1989).
- ²⁰DIHI-D team, in Ref. 9, p. 69.
- ²¹JET team, in Ref. 9, p. 27.
- ²²R. J. Goldston, G. Bateman, W. A. Houlberg, S. M. Kaye, G. H. Neilson, F. W. Perkins, N. Pomphrey, M. Porkolab, K. S. Reidel, R. D. Stambaugh, D. P. Stotler, R. E. Waltz, and M. C. Zarnstorff, in Ref. 18, p. 93.
- ²³K. Tomabechi, in Ref. 9, Vol. 3, p. 217.
- ²⁴K. Bol, V. Arunasalam, M. Bitter, D. Boyd, K. Brau, N. Bretz, J. Bussac, S. Cohen, P. Colestock, S. Davis, D. Dimock, F. Dylla, D. Eames, P. Efthimion, H. Eubank, R. J. Goldston, R. J. Hawryluk, K. W. Hill, E. Hinno, J. Hosea, H. Hsuan, F. Jobs, D. Johnson, E. Mazzucato, S. Medley, E. Meserve, N. Sauthoff, G. Schmidt, F. Stauffer, W. Stodiek, J. Strachan, S. Suckewer, G. Tait, M. Ulrickson, and S. von Goeler, in *Plasma Physics and Controlled Nuclear Fusion Research, 1978*, Proceedings of the Seventh International Conference, Innsbruck (International Atomic Energy Agency, Vienna, 1979), Vol. 1, p. 11.
- ²⁵S. Fairfax, A. Gondhalekar, R. Granetz, M. Greenwalt, D. Gwinn, I. H. Hutchinson, S. E. Kissel, B. Lipschultz, E. S. Marmar, D. O. Oversek, D. S. Pappas, J. Parker, R. R. Parker, P. A. Pribyl, J. E. Rice, J. J. Schuss, N. Sharky, R. J. Temkin, J. L. Terry, R. Watterson, S. M. Wolfe, S. L. Allen, J. Castracane, and W. Hodge, in *Plasma Physics and Controlled Nuclear Fusion Research, 1980*, Proceedings of the Eighth International Conference, Brussels (International Atomic Energy Agency, Vienna, 1979), Vol. 1, p. 439.
- ²⁶R. E. Waltz, J. C. DeBoo, M. N. Rosenbluth, C. W. Barnes, R. J. Goldston, F. W. Perkins, S. D. Scott, and M. C. Zarnstorff, in Ref. 9, Vol. 2, p. 273.
- ²⁷R. E. Waltz, J. C. DeBoo, and M. N. Rosenbluth, *Phys. Rev. Lett.* **65**, 2390 (1990).
- ²⁸J. C. DeBoo, R. E. Waltz, and T. Osborne, in Ref. 18, p. 173.
- ²⁹R. E. Waltz, J. C. DeBoo, and T. H. Osborne, *Nucl. Fusion* **32**, 1051 (1992).
- ³⁰Y. Kamada, R. T. Snider, T. S. Taylor, E. J. Strait, and J. R. Ferron, "Sawtooth frequency studies in the DIII-D tokamak," to appear in *Nucl. Fusion*.
- ³¹C. K. Phillips, A. Cavallo, P. L. Colestock, D. N. Smithe, G. J. Greene, G. W. Hammett, J. C. Hosea, J. E. Stevens, and J. R. Wilson, in *Radio-Frequency Power in Plasmas*, edited by R. MacWilliams, Proceedings of the 8th Topical Conference, Irvine, CA (American Institute of Physics, New York, 1989), p. 310.
- ³²G. Rewoldt, W. M. Tang, and M. S. Chance, *Phys. Fluids* **25**, 480 (1982).
- ³³R. Marchand, W. M. Tang, and G. Rewoldt, *Phys. Fluids* **23**, 1164 (1980); P. H. Diamond and H. Biglari, *Phys. Rev. Lett.* **65**, 2865 (1990).
- ³⁴G. S. Lee and P. H. Diamond, *Phys. Fluids* **29**, 3291 (1986).
- ³⁵W. Horton, *Phys. Rep.* **192**, 1 (1990).
- ³⁶E. A. Frieman and L. Chen, *Phys. Fluids* **25**, 502 (1982).
- ³⁷J. W. Connor, *Nucl. Fusion* **26**, 193 (1986).
- ³⁸F. Y. Gang, P. H. Diamond, and M. N. Rosenbluth, *Phys. Fluids B* **3**, 68 (1991); T. S. Hahm and W. M. Tang, *ibid.* **3**, 989 (1991).
- ³⁹L. Chen and C. Z. Cheng, *Phys. Fluids* **23**, 2242 (1980); R. J. Hastie, K. W. Hesketh, and J. B. Taylor, *Nucl. Fusion* **19**, 1223 (1979); P. L. Similon and P. H. Diamond, *Phys. Fluids* **27**, 916 (1984).
- ⁴⁰R. J. Goldston, G. Bateman, M. G. Bell, R. Bickerton, E. A. Chaniotakis, D. R. Cohn, P. L. Colestock, D. H. Hill, W. A. Houlberg, S. C. Jardin, S. S. Medley, G. H. Neilson, W. A. Peebles, F. W. Perkins, N. Pomphrey, M. Porkolab, J. A. Schmidt, D. J. Sigmar, R. D. Stambaugh, D. P. Stotler, M. Ulrickson, R. E. Waltz, and K. M. Young, in Ref. 17, Vol. 1, p. 134.
- ⁴¹F. X. Söldner, E. R. Müller, F. Wagner, H. S. Bosch, A. Eberhagen, H. U. Farbach, G. Fussmann, O. Gehre, K. Gentle, J. Gernhardt, O. Gruber, W. Herrmann, G. Jameschitz, M. Kornherr, K. Krieger, H. M. Mayer, K. McCormick, H. D. Murmann, J. Neuhauser, R. Nolte, W. Poschenrieder, H. Röhr, K.-H. Steuer, U. Stroth, N. Tsois, and H. Verbeek, *Phys. Rev. Lett.* **61**, 1105 (1988); M. Bessenrodt-Weberpals, K. McCormick, F. X. Söldner, F. Wagner, H. S. Bosch, O. Gehre, E. R. Müller, H. D. Murmann, J. Neuhauser, W. Poschenrieder, K.-H. Steuer, N. Tsois, and the ASDEX team, *Nucl. Fusion* **31**, 155 (1991).
- ⁴²R. K. Janev, W. D. Langer, K. Evans, Jr., and D. E. Post, Jr., *Elementary Processes in Hydrogen-Helium Plasmas* (Springer-Verlag, New York, 1987).
- ⁴³D. L. Book, *NRL Plasma Formulary* (Naval Research Laboratory, Washington, DC, 1987).
- ⁴⁴D. R. Thayer and P. H. Diamond, *Phys. Fluids* **30**, 3724 (1987).
- ⁴⁵A. S. Ware, P. H. Diamond, H. Biglari, B. A. Carreras, L. A. Charlton, J.-N. Lebouef, and A. J. Wootton, *Phys. Fluids B* **4**, 877 (1992).
- ⁴⁶Y. Z. Zhang and S. M. Mahajan, *Phys. Fluids B* **4**, 207 (1992).
- ⁴⁷J.-N. Lebouef, D. K. Lee, B. A. Carreras, N. Dominguez, J. H. Harris, C. L. Hedrick, C. Hildago, J. A. Holmes, J. Ruitter, P. H. Diamond, A. S. Ware, Ch. P. Ritz, A. J. Wootton, W. L. Rowan, and R. V. Bravenac, *Phys. Fluids B* **3**, 2291 (1991).

- ⁴⁸S. M. Kaye, C. W. Barnes, M. G. Bell, J. C. DeBoo, M. Greenwald, K. Riedel, D. Sigmar, N. Uckan, and R. Waltz, *Phys. Fluids B* **2**, 2926 (1990).
- ⁴⁹P. H. Yushmanov, T. Takizuka, K. S. Riedel, O. J. W. F. Kardaun, J. G. Cordey, S. M. Kaye, and D. E. Post, *Nucl. Fusion* **30**, 1999 (1990).
- ⁵⁰J. P. Christiansen, J. G. Cordey, O. J. W. F. Kardaun, and K. Thomsen, *Nucl. Fusion* **31**, 2117 (1991).
- ⁵¹F. W. Perkins and Y. C. Sun, in *Basic Physical Processes of Toroidal Fusion Plasma*, edited by G. P. Lampis, M. Lontano, G. G. Leotta, A. Malein, and E. Sindoni (Euratom, Brussels, 1986), Vol. 2, p. 587.
- ⁵²R. R. Dominguez and R. E. Waltz, *Nucl. Fusion* **27**, 65 (1987).
- ⁵³M. C. Zarnstorff, V. Arunasalam, C. W. Barnes, M. G. Bell, M. Bitter, H.-S. Bosch, N. L. Bretz, R. Budny, C. E. Bush, A. Cavallo, T. K. Chu, S. A. Cohen, P. L. Colestock, S. L. Davis, D. L. Dimock, H. F. Dylla, P. C. Efthimion, A. B. Ehrhardt, R. K. Fonck, E. D. Fredrickson, H. P. Furth, G. Gammel, R. J. Goldston, G. J. Green, B. Grek, L. R. Grisham, G. W. Hammett, R. J. Hawryluk, H. W. Hendel, K. W. Hill, E. Hinnov, J. C. Hosea, R. B. Howell, H. Hsuan, R. A. Hulse, K. P. Jaehnig, A. C. Janos, D. L. Jassby, F. C. Jobs, D. W. Johnson, L. C. Johnson, R. Kaita, C. Kieras-Phillips, S. J. Kilpatrick, V. A. Krupin, P. H. LaMarche, B. LeBlanc, R. Little, A. I. Lysojvan, D. M. Manos, D. K. Mansfield, E. Mazzucato, R. T. McCann, M. P. McCarthy, D. C. McCune, K. M. McGuire, D. H. McNeill, D. M. Meade, S. S. Medley, D. R. Mikkelsen, R. W. Motley, D. Mueller, Y. Murakami, J. A. Murphy, E. B. Nieschmidt, D. K. Owens, H. K. Park, A. T. Ramsey, M. H. Redi, A. L. Roquemore, P. H. Rutherford, T. Saito, N. R. Sauthoff, G. Schilling, J. Schivell, G. L. Schmidt, S. D. Scott, J. C. Sinis, J. E. Stevens, W. Stodiek, J. D. Strachan, B. C. Stratton, G. D. Tait, G. Taylor, J. R. Timberlake, H. H. Towner, M. Ulrickson, S. von Goeler, R. M. Wieland, M. D. Williams, J.-R. Wilson, K.-L. Wong, S. Yoshikawa, K. M. Young, and S. J. Zweben, in *Plasma Physics Controlled Nuclear Fusion Research, 1988*, Proceedings of the Twelfth International Conference, Nice (International Atomic Energy Agency, Vienna, 1989), Vol. 1, p. 183.
- ⁵⁴R. J. Fonck, D. S. Darrow, and K. P. Jaehnig, *Phys. Rev. A* **29**, 3288 (1984).
- ⁵⁵R. J. Goldston, *Plasma Physics Controlled Nucl. Fusion Res.* **26**, 87 (1984).
- ⁵⁶P.-H. Rebut, M. L. Watkins, D. J. Gambier, and D. Boucher, *Phys. Fluids B* **3**, 2209 (1991).
- ⁵⁷M. C. Zarnstorff, K. McGuire, M. G. Bell, B. Grek, D. Johnson, D. McCune, H. Park, A. Ramsey, and G. Taylor, *Phys. Fluids B* **2**, 1852 (1990).
- ⁵⁸C. Barnes and S. Scott (private communication, 1992).
- ⁵⁹D. P. Schissel, K. H. Burrell, J. C. DeBoo, R. J. Groebner, A. G. Kellman, N. Ohya, T. H. Osborne, M. Shimada, R. T. Snider, R. D. Stambaugh, T. S. Taylor, and the DIII-D research team, *Nucl. Fusion* **29**, 185 (1989).
- ⁶⁰J. G. Cordey, D. V. Bartlett, V. Bhatnagar, R. J. Bickerton, M. Bures, J. D. Callen, D. J. Campbell, C. D. Callis, J. P. Christiansen, S. Corti, A. E. Costley, G. A. Cottrell, G. Duesing, J. Fessey, M. Gadeberg, A. Gibson, A. Gondhalekar, N. A. Gottardi, C. W. Gowers, M. Von Hellermann, F. Hendriks, L. Horton, H. Jäckel, J. Jacquinet, O. N. Jarvis, T. T. C. Jones, E. Källne, J. Källne, M. Keilhacker, S. Kissel, L. De Kock, P. Lallia, E. Lazzaro, P. J. Lomas, N. Lopes-Cardozo, P. D. Morgan, P. Nielsen, J. O'Rourke, R. Prentice, R. T. Ross, G. Sadler, F. C. Schüller, A. Stabler, P. Smeulders, M. F. Stamp, D. Stork, P. E. Stott, D. R. Summers, A. Tanga, P. R. Thomas, E. Thompson, K. Thomsen, G. Tonetti, B. J. Tubbing, and M. L. Watkins, in *Plasma Physics Controlled Nuclear Fusion Research, 1986*, Proceedings of the Eleventh International Conference, Kyoto (International Atomic Energy Agency, Vienna, 1987), Vol. 1, p. 99.
- ⁶¹R. J. Hawryluk, V. Arunasalam, C. W. Barnes, M. Beer, M. Bell, R. Bell, H. Biglari, M. Bitter, R. Boivin, N. L. Bretz, R. Budny, C. W. Bush, C. Z. Cheng, T. K. Chu, S. A. Cohen, S. Cowley, P. C. Efthimion, R. J. Fonck, E. Fredrickson, H. P. Furth, R. J. Goldston, G. Green, B. Grek, L. R. Grisham, G. Hammett, W. Heidbrink, K. W. Hill, J. Hosea, R. A. Hulse, H. Hsuan, A. Janos, D. Jassby, F. C. Jobs, D. W. Johnson, L. C. Johnson, J. Kesner, C. Kieras-Phillips, S. J. Kilpatrick, H. Kugel, P. H. LaMarche, B. LeBlanc, D. M. Manos, D. K. Mansfield, E. S. Marmor, E. Mazzucato, M. P. McCarthy, M. Mauel, D. C. McCune, K. M. McGuire, D. M. Meade, S. S. Medley, D. R. Mikkelsen, D. Monticello, R. Motley, D. Mueller, Y. Nagayama, G. A. Navratil, R. Nazikian, D. K. Owens, H. Park, W. Park, S. Paul, F. Perkins, S. Pitcher, A. T. Ramsey, M. H. Redi, G. Rewoldt, D. Roberts, A. L. Roquemore, P. H. Rutherford, S. Sabbagh, G. Schilling, J. Schivell, G. L. Schmidt, S. D. Scott, J. Snipes, J. Stevens, J. D. Strachan, B. C. Stratton, W. Stodiek, E. Synakowski, Y. Takase, W. Tang, G. Taylor, J. Terry, J. R. Timberlake, H. H. Towner, M. Ulrickson, S. von Goeler, R. Wieland, M. Williams, J. R. Wilson, K. L. Wong, M. Yamada, S. Yoshikawa, K. M. Young, M. C. Zarnstorff, and S. J. Zweben, *Plasma Phys. Controlled Fusion* **33**, 1509 (1991).
- ⁶²D. P. Schissel, J. C. DeBoo, K. H. Burrell, J. R. Ferron, R. J. Groebner, H. St. John, R. D. Stambaugh, the DIII-D research team, B. J. D. Tubbing, K. Thomsen, J. G. Cordey, M. Keilhacker, D. Stork, P. E. Stott, A. Tanga, and the JET team, *Nucl. Fusion* **31**, 73 (1991).
- ⁶³K. S. Riedel, *Nucl. Fusion* **30**, 755 (1990).